

Contents lists available at ScienceDirect

Petroleum Science

journal homepage: www.keaipublishing.com/en/journals/petroleum-science



Original Paper

Mg-C-O isotopes and elements reveal the origin of dolostone in the Middle Jurassic Buqu Formation



Xi Li ^{a, b}, An-Jiang Shen ^{a, b, *}, Rui-Lin Hao ^c

- ^a Key Laboratory of Carbonate Reservoirs, CNPC, Hangzhou, 310023, Zhejiang, China
- ^b PetroChina Hangzhou Research Institute of Geology, Hangzhou, 310023, Zhejiang, China
- ^c Friedrich-Alexander Universität Erlangen-Nürnberg, GeoZentrum Nordbayern, Erlangen, D-91054, Germany

ARTICLE INFO

Article history: Received 6 May 2024 Received in revised form 21 August 2024 Accepted 11 November 2024 Available online 14 November 2024

Edited by Jie Hao

Keywords:
Origin of dolostone
Mg-C-O isotopes
Sea level changes
Burial adjustment dolomitization
Buqu formation
Plateau basin

ABSTRACT

The origin of dolostone in the Middle Jurassic Buqu Formation of the Plateau Basin has been a subject of prolonged debate. This study combines detailed petrological observations with analyses of Mg-C-O isotopes and elements to constrain the origin of dolostones in the Buqu Formation. Petrography and cathodoluminescence (CL) examination identified three types of matrix dolostones: very finely to finely crystalline dolostone (D1), finely to medium crystalline dolostone (D2), and medium to coarsely crystalline dolostone (D3). The analysis of the diagenesis sequence reveals that D1 originated from the dolomitization of grainstone in the early diagenetic phase, whereas D2 and D3 resulted from the recrystallization of D1 during the later burial phase. The presence of high Na (>100 ppm), low Fe (<1000 ppm), low Mn (<250 ppm), positive Ce anomaly, LREE enrichment, stable δ^{26} Mg (-2.28‰ to -2.04%), and δ^{13} C (1.02% - 2.95%) indicates that the early dolomitization fluid was oxidized seawater. As the crystal size increases ($D1 \rightarrow D2 \rightarrow D3$), the progressively rising Mn content and significantly negative δ^{18} O (-10.72% to -7.81%) suggest that the dolostone has experienced modification and alteration by buried pore water in the later stages. The fluctuations in relative sea level during the sedimentary deposition of the Buqu Formation were reconstructed through the utilization of Na, Sr/Cu, Sr/Ba, Rb/Sr, \sum REE, and δ^{13} C. It was observed that the δ^{26} Mg of dolostone closely mirrored the variations in sea level. The consistent trend of change confirms that sea level fluctuations control the formation and distribution of early dolostone. Frequent sea level rise and fall prompted the limestone deposited on the carbonate platform to be continuously transformed into dolostone, which accumulates over a long period to form large-scale thick dolostone. After the formation entered the burial stage, under the combined action of high Mg/Ca ratio pore water, high temperature, and high pressure, the early dolostone experienced the adjustment of burial dolomitization. This research offers a typical case study on the application of Mg-C-O isotope and elements to determine the origin of dolostone. This will aid in a more comprehensive understanding of the formation process of dolostone in ancient rock records. © 2024 The Authors. Publishing services by Elsevier B.V. on behalf of KeAi Communications Co. Ltd. This is an open access article under the CC BY license (http://creativecommons.org/licenses/by/4.0/).

1. Introduction

Dolostone is widely distributed in ancient carbonate rock strata globally and frequently exhibits excellent pore structure, rendering it among the foremost reservoir rocks for oil and gas exploration (Ma et al., 2008; Wang et al., 2023). Despite the Mg/Ca ratio of modern seawater favors substantial dolomite precipitation, dolomite is conspicuously scarce in modern marine environments (Warren, 2000). Moreover, synthesizing dolomite under inorganic

* Corresponding author.

E-mail address: shenaj_hz@petrochina.com.cn (A.-]. Shen).

low-temperature conditions, even in supersaturated solutions, is challenging (Land, 1998; Gregg et al., 2015). The conflicting ancient and modern geological records, coupled with unsuccessful attempts to synthesize dolomite at low temperatures, have engendered numerous mysteries surrounding the genesis of dolostone (Ryb and Eiler, 2018; Cai et al., 2021).

The Plateau Basin is recognized as mainland China's largest Mesozoic marine oil and gas enrichment basin (Wang et al., 2024). The Middle Jurassic Buqu Formation contains extensive dolostone strata spanning thousands of square kilometers, with sediment thickness exceeding hundreds of meters. These dolostones are considered highly promising oil and gas reservoirs in the region (Fu

et al., 2016; Wang et al., 2022). To form such widely distributed and massive dolostones, a substantial and sustained supply of dolomitization fluids is required. However, the potential sources of fluids capable of instigating dolomitization are diverse, encompassing seawater (Ryan et al., 2020), buried pore water (Jiang et al., 2016), and magmatic-hydrothermal fluid (Koeshidayatullah et al., 2020). Moreover, these fluids not only act independently to induce dolomitization but may also amalgamate sequentially to carry out multi-phase dolomitization processes (Zhao et al., 2018). Following the deposition of the Middle Jurassic Bugu Formation, the Plateau Basin experienced successive Late Yanshanian and Himalayan tectonic movements (Ma et al., 2017). Structural uplifts facilitated the ascent of meteoric water or thermally driven fluids along tectonic fissures, exacerbating the challenge of precisely discerning the fluid sources responsible for dolomitization. Consequently, the origin of Bugu Formation dolostone has been a subject of protracted debate (Liu et al., 2008; Yi et al., 2014; Wan et al., 2020).

The dolostones that result from different fluid conditions exhibit distinct geochemical signatures of elements and isotopes. The analysis of element content and isotope composition in dolostone is essential for identifying the origins of dolomitization fluids (Clayton and Jones, 1968; Fritz and Smith, 1970; Kretz, 1982). Traditional analyses of element content and C-O isotope composition have been widely utilized as effective indicators for recognizing the sources of dolomitization fluids (Bi et al., 2018; Adams et al., 2019). Recent advancements in the accuracy of Mg isotope measurements have enabled more precise constraints on the Mg isotope composition of potential dolomitization fluids such as seawater, buried pore water, and magmatic-hydrothermal fluids (Foster et al., 2010; Jacobson et al., 2010; Beinlich et al., 2014; Higgins and Schrag, 2015). The systematic study of elements and C-O-Mg isotopes in dolostone can help in determining the sources of dolomitization fluids in a specific area (Bialik et al., 2018; Kimmig et al., 2021). It is important to note that whole-rock geochemical analysis often fails to ensure the accuracy of dolostone geochemical information due to various contaminants such as terrigenous clasts, calcite cements, and hydrothermal minerals. These contaminants can alter the element content and C-O-Mg isotope composition data of dolostone, leading to spatial variations in geochemical characteristics within the same sample (Frimmel, 2009; Baldwin et al., 2011).

To ensure the reliability of geochemical data, this study initially analyzed the petrological characteristics of dolostone samples using optical microscopy and cathodoluminescence (CL). Subsequently, pure dolostone powder was obtained with a handheld dental drill to analyze element content and C-O-Mg isotopic composition. After effectively assessing the reliability of geochemical signals, the study successfully traced the source of the fluid responsible for the dolomitization of the Buqu Formation and established a rational dolomitization model, thereby revealing the origin of the Buqu Formation dolostone. The findings of this research are particularly significant for the exploration of dolostone oil and gas reservoirs in the Plateau Basin. Furthermore, this study serves as a representative case demonstrating the application of Mg-C-O isotopes and elemental analysis in determining the origin of dolostones.

2. Geological background

The Plateau Basin, a high-altitude basin abundant in oil and gas resources, is situated in northern Tibet, China, covering a substantial area of approximately 22×10^4 km² (Fu et al., 2013). Geotectonically, the Plateau Basin is located in the eastern segment of the Tethys-Himalayan tectonic region, lying between the Kokoxili-Jinsha River and the Bangong Lake-Nujiang River suture zones

(Zhu et al., 2013) (Fig. 1(a)).

During the Mesozoic era, the geological evolution of the Plateau Basin was significantly influenced by the subduction of the Paleo-Tethys Ocean and the expansion of the Meso-Tethys Ocean (Pullen et al., 2008). The terrane detached from the northeastern margin of the Gondwana supercontinent from the Late Carboniferous to the Early Permian period. This detachment was a result of intercontinental rifts, leading to the formation of the Paleo-Tethys Ocean, which existed until the Late Permian (Golonka, 2007). Subsequently, the northward subduction of the terrane caused the closure of the Paleo-Tethys Ocean and the subsequent expansion of the Meso-Tethys Ocean, culminating in the closure of the limited ocean between the northern and southern terranes (Cheng et al., 2012). In the Late Triassic period, the collision between the southern and northern Plateau terranes resulted in the closure of the ocean basin and the emergence of the Central Uplift zone (Ma et al., 2017; Lai et al., 2019).

Upon entering the Jurassic period, the Plateau Basin underwent a transition from a compressional to an extensional environment as a result of the reopening of the ocean basin. This transition marked the initiation of large-scale marine sedimentation in the Plateau Basin during the Mesozoic (Pan et al., 2012). The sedimentation of the Middle Jurassic Bugu Formation in the Plateau Basin was characterized by a continuous and stable subsidence phase. Simultaneously, the expansion of the oceanic basin led to the intrusion of seawater from the south to the north, causing widespread basin inundation and subsequent sedimentation of extensive carbonate rock sequences (Ma et al., 2023). In the Southern Plateau Basin, the sedimentation of the Middle Jurassic Bugu Formation occurred within an intra-platform shoal sedimentary environment, marked by the development of east-west trending layered dolostones (Fig. 1(b)). The lithology reveals multiple cycles of limestone-dolostone stacking (Wan et al., 2017) (Fig. 1(c)). Following deposition, the Buqu Formation underwent rapid burial, reaching a maximum burial depth of approximately 4000 m (Xu and Qin, 2004). The Buqu Formation experienced sequential tectonic movements during the burial phase, including the Late Yanshanian, Himalayan, and Qinghai-Tibetan Plateau uplift events (Xia et al., 2016).

3. Sample collection and methods

3.1. Sample collection

A total of 40 dolostone samples were acquired from the depth range of 20.1~m-37.95~m of Well ZK-1 in the Plateau Basin, situated along the Geluguanna profile. The collected samples were divided into two portions. One portion was processed into thin sections for petrological and cathodoluminescence analyses, while the other portion was cut into thick slabs (approximately 2 cm) for powder collection. Powder samples were obtained using a handheld dental drill to analyze the element content and C-O-Mg isotope composition.

3.2. Petrological analysis

All experiments in this study were conducted at the National Key Laboratory of Energy Carbonate Oil and Gas, CNPC. Thin sections were examined and photographed using a Leica DM 2500P optical microscope. Cathodoluminescence observation and imaging were conducted using a CL8200MK cathodoluminescence instrument, with an operating beam voltage ranging from 10 to 15 kV and a beam current of 400–500 mA.

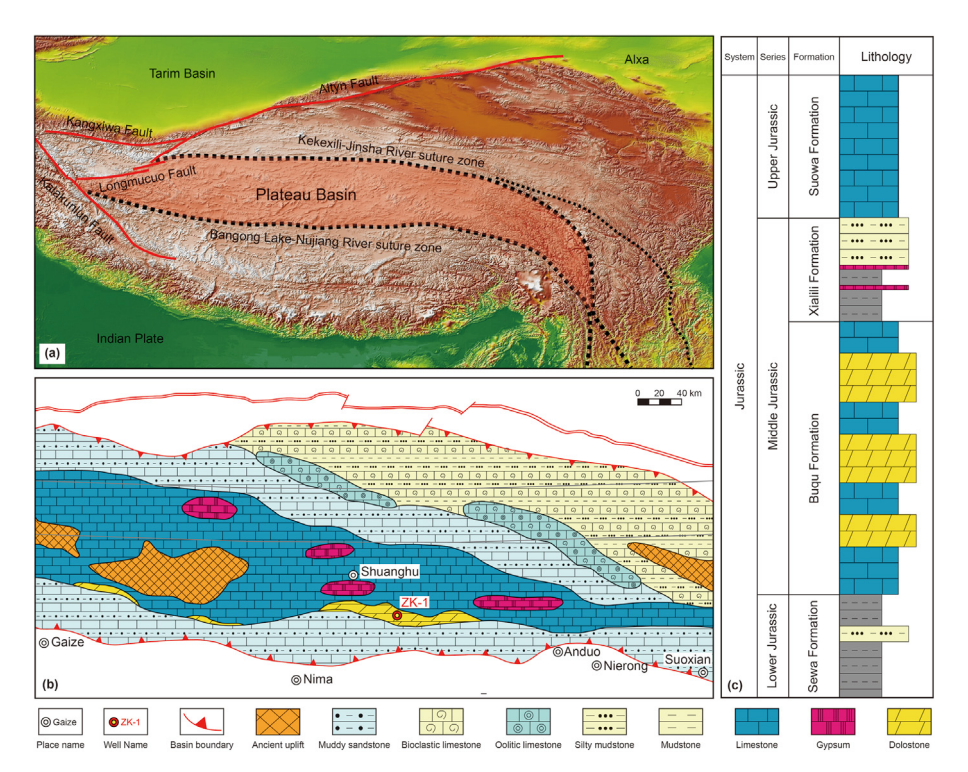


Fig. 1. (a) Geographical location of the Plateau Basin; (b) Lithofacies paleogeography of the Middle Jurassic Buqu Formation (Ma et al., 2023); (c) Lithology of the Middle Jurassic Buqu Formation.

3.3. Geochemical analysis

3.3.1. Element content analysis

The analysis of elemental content necessitates approximately 50 mg of powder. A procedure involving the gradual addition of 1 mL of pure nitric acid (HNO₃) and 1 mL of high-purity hydrofluoric acid (HF) is followed by subjecting the mixture to a 190 °C oven for a minimum of 24 h. Subsequently, 1 mL of pure HNO₃ is added, and the solution is evaporated once more. This is succeeded by the addition of 1 mL of high-purity HNO₃ and 1 mL of deionized water. The mixture is then placed in an oven at 190 °C for at least 12 h. The solution is eventually transferred to a polyethylene bottle and diluted to 100 mL with 2% HNO₃. The elemental content of the prepared samples was determined using the iCAP TQ ICP-MS instrument.

3.3.2. C-O isotope analysis

C-O isotope analysis necessitates approximately 10 mg of powder. The sample undergoes a reaction with anhydrous phosphoric acid at 50 °C for 4 h to ensure the complete release of CO $_2$ from the dolostone. Subsequently, the analysis is conducted using a Delta V Advantage isotope ratio mass spectrometer. The measured isotope ratios are reported relative to the V-PDB standard. The obtained results are compared with the GBW4405 and GBW4406 standard samples. The long-term measurement precision for $\delta^{13}\text{C}$ and $\delta^{18}\text{O}$ is $\pm 0.06\%$ and $\pm 0.08\%$, respectively.

3.3.3. Mg isotope analysis

The analysis of Mg isotopes necessitates approximately 20 mg of powder. The powder is dissolved in 5 mL of 0.5 N acetic acid and subsequently treated with ultrasound for 2 h, followed by a 24-h leave period. Following centrifugation at 4000 rpm for 15 min, the resulting supernatant is transferred to a clean test tube and evaporated to dryness on an electric heating plate at 140 °C. The

sample is reconstituted in 200 µL of 1N HNO₃ and then desiccated once more. After standing for 24 h, the Bio-Rad AG50W-X8 resin (200–400 mesh) is used to separate magnesium from other elements. Following purification, the ratios of Ca/Mg, Al/Mg, Na/Mg, K/Mg, and Fe/Mg are all below 5%, with the recovery rate for each sample exceeding 95%.

The Mg isotope was analyzed using the Neptune Plus multicollector inductively coupled plasma mass spectrometer. To rectify instrumental fractionation, a standard-sample-standard cross-calibration technique was applied. Each sample was analyzed at least four times. All data were standardized to the international Mg isotope standard (DSM-3) values and expressed using the δ notation to represent the Mg isotope composition of dolostone (Galy et al., 2003) (Eqs. (1) and (2)). The measured $\delta^{26} \text{Mg}_{\text{JDO-1}}$ value was $-2.34\% \pm 0.05\%$, which is consistent with the laboratory's long-term stable value of $-2.37\% \pm 0.04\%$ (Bao et al., 2020).

$$\begin{split} \delta^{26}\text{Mg (\%)} &= (^{26}\text{Mg})^{24}\text{Mg}_{sample} - ^{26}\text{Mg}/_{24}\text{Mg}_{DSM-3})/\\ (^{26}\text{Mg})^{24}\text{Mg}_{DSM-3}) \times 1000 \end{split} \tag{1}$$

$$\delta^{25} Mg \text{ (\%)} = (^{25} Mg/^{24} Mg_{sample} - ^{25} Mg/^{24} Mg_{DSM-3})/$$

$$(^{25} Mg/^{24} Mg_{DSM-3}) \times 1000$$
 (2)

4. Results

4.1. Petrology

The Buqu Formation, as observed in the Geluguanna profile, is characterized by alternating layers of limestone and dolostone. Lithological analysis has revealed multiple sedimentary cycles, with dolostone predominantly present in the upper parts of these cycles (Fig. 2(a)). Both limestone and dolostone contain abundant bioclasts of gastropods and/or bivalves (Fig. 2(b)). The classification of

matrix dolostone samples from the Buqu Formation in Well ZK-1 into three types—very finely to finely crystalline dolostone (D1), finely to medium crystalline dolostone (D2), and medium to coarsely crystalline dolostone (D3) was based on the size of dolomite crystals and the characteristics of the boundaries observed through thin section and cathodoluminescence analyses (Gregg and Sibley, 1984; Sibley and Gregg, 1987).

The crystal size of dolomite in D1 ranges from 30 to 250 μ m, with predominantly euhedral or subhedral crystal morphology. D1 contains numerous leached pores and intercrystalline pores, some of which are filled with sparry calcite cement (Fig. 2(c), (d)). The CL image of D1 reveals that the center of dolomite crystals is darker than the edges (Fig. 2(e)). In D2, dolomite sizes range from 100 to 500 μ m, with crystal morphology typically being planar euhedral to subhedral (Fig. 2(f)). Following the restoration of the primary rock texture in D2, various residual granular structures are visible, along with the development of intercrystalline pores, leached pores, and moldic pores (Fig. 2(g)). D2 exhibits a moderate intensity of CL, appearing as a dark red color (Fig. 2(h)). Dolomite crystals in D3 are

larger, ranging from 250 to 1000 μm . The crystal morphology often presents as curved subhedral or anhedral, maintaining a residual grainstone texture (Fig. 2(i)). Dolomite in D3 primarily contacts each other through concave and convex curved surfaces, with well-developed melodic pores (Fig. 2(j)). D3 displays strong CL, appearing as a dark red color, and shows banded CL features with alternating light and dark bands along the edges of the dolomite (Fig. 2(k)).

4.2. Geochemistry

Please refer to Tables 1 and 2 for the geochemical data detailing element content and C-O-Mg isotope composition. The Na content ranges from 114 to 266 ppm, while the Mn/Sr ratio varies from 1.51 to 7.99 (Fig. 3(a)). The Mn content varies from 71 to 257 ppm. The Fe content ranges from 368 to 1748 ppm (Fig. 3(b)). The Ba content in D1, D2, and D3 is relatively low, with average values of 8.07, 6.66, and 11.07 ppm, respectively, as presented in Fig. 3(c). Following PASS normalization, the δ Ce values range from 1.09 to 3.45, and the

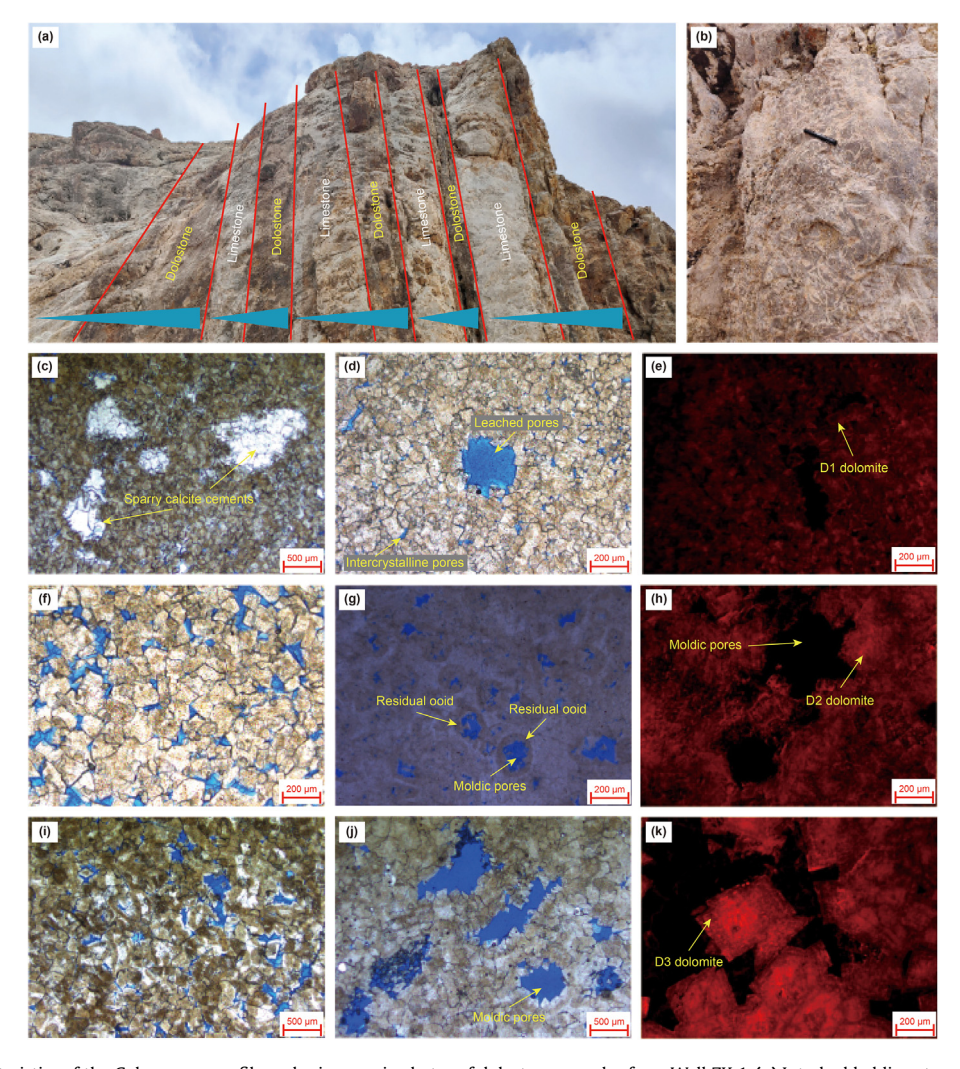


Fig. 2. Macroscopic characteristics of the Geluguanna profile and microscopic photos of dolostone samples from Well ZK-1. (a) Interbedded limestone and dolostone, Geluguanna profile; (b) Bioclasts of gastropods and/or bivalves, Geluguanna profile; (c) Very finely to finely crystalline dolostone (D1), freshwater cements, ZK-1-28, viewed under plane polarized light; (d) D1, numerous intercrystalline and leached pores, ZK-1-23, viewed under plane polarized light; (e) D1, exhibits weak dark red light, ZK-1-15, observed through cathodoluminescence; (f) Finely to medium crystalline dolostone (D2), dolomite crystals are euhedral or subhedral, ZK-1-25, viewed under plane polarized light; (g) D2, numerous residual granular structures, ZK-1-25, viewed under plane polarized light; (h) D2, exhibits dark red light with moderate intensity, ZK-1-25, observed through cathodoluminescence; (i) Medium to coarsely crystalline dolostone (D3), the size of dolomite crystals ranges from 250 to 1000 μm, ZK-1-26, viewed under plane polarized light; (j) D3, numerous moldic pores, ZK-1-13, viewed under plane polarized light; (k) D3, strong dark red light, with the edges of dolomite crystals displaying ring-like luminescence, ZK-1-26, observed through cathodoluminescence.

Table 1Analysis data of Mg-C-O isotopes and trace elements in the dolostone of the Buqu Formation of the Middle Jurassic.

Alidiysis uat									•					C /D	4000+P1 /		I DEE/	2.0	
Number L	epth, m	Lithology	o ²⁰ Mg, %	o 2SD 0)13C, ‰	δ ¹⁰ O, ‰	Na, pp	m Sr, ppn	ı Mn, ppm	i Min/ Sr	Fe, ppm	ı Ba, ppm	Sr/Cu	Sr/Ba	1000*Rb/ Sr	ΣREE	HREE	δCe	ðEU
	_				_		_												
ZK-1-1 2		D2	-2.23	0.02 2		-9.08	219	35	124	3.49	497	12.10				1.12			0.35
ZK-1-2 2		D2	-2.17	0.04 2		-9.23	266	39	257	6.56	1279	10.30	63.61			1.27		1.82	0.23
ZK-1-3 2	20.85	D1	-2.14	0.03 1	1.39	-10.34	204	28	152	5.35	894	19.59	31.05			0.80	4.66	1.49	1.00
ZK-1-4 2	21.50	D2	-2.22	0.03 2	2.15	-9.47	197	37	253	6.93	487	3.47	41.72	10.53	2.70	1.21	8.09	1.42	0.39
ZK-1-5 2		D2	-2.17	0.02 1		-9.90	190	33	202	6.07	646	8.72	43.77			0.85			0.44
ZK-1-6 2		D1	-2.13	0.01 2	2.88	-8.98	234	30	152	5.11	525	16.21	73.16	1.83	5.14	0.71		2.20	1.14
ZK-1-7 2	23.00	D3	-2.18	0.02 1	1.82	-10.12	207	41	221	5.43	753	9.19	49.72	4.42	1.72	0.93	6.46	2.27	0.69
ZK-1-8 2	23.85	D2	-2.20	0.04 2	2.59	-9.05	243	33	230	7.07	443	10.01	31.31	3.25	2.39	0.88	4.75	1.66	0.74
ZK-1-9 2	24.25	D2	-2.23	0.02 2	2.35	-9.38	252	36	208	5.73	391	9.71	35.39	3.75	1.77	1.01	5.35	3.12	0.78
ZK-1-10 2	24.45	D2	-2.23	0.01 2	2.48	-8.97	260	31	177	5.65	425	13.83	98.06	2.26	2.69	0.88	5.60	2.32	0.77
ZK-1-11 2	24.80	D1	-2.27	0.04 1	1.99	-9.61	225	43	121	2.80	531	21.98	75.90	1.97	2.68	0.74	4.86	1.68	0.85
ZK-1-12 2	25.10	D3	-2.21	0.01 2		-8.44	205	40	108	2.69	463	14.07	108.67			0.94		2.00	0.69
ZK-1-13 2	25.30	D3	-2.19	0.04 2	2.63	-9.25	247	36	231	6.33	502	11.67	78.34	3.12	2.13	0.73	4.38	2.21	0.78
ZK-1-14 2	25.80	D1	-2.16	0.03 2	2.34	-9.03	185	36	132	3.69	622	5.56	54.97	6.45	3.21	0.87	5.69	1.73	0.64
ZK-1-15 2	26.30	D1	-2.04	0.04 2	2.87	-9.06	214	32	134	4.20	536	6.16	82.33	5.18	4.76	0.75	4.97	2.13	0.70
ZK-1-16 2	26.95	D1	-2.10	0.01 2	2.95	-8.91	202	31	135	4.36	509	3.19	73.01	9.71	4.93	0.57	3.57	1.09	0.53
ZK-1-17 2	27.35	D1	-2.15	0.02 2	2.65	-8.80	210	33	103	3.17	497	9.71	82.54	3.36	2.12	1.36	9.13	1.36	0.69
ZK-1-18 2	27.90	D1	-2.23	0.04 2	2.25	-9.15	206	33	126	3.87	651	3.11	35.49	10.51	3.45	0.63	4.39	1.71	0.66
ZK-1-19 2	28.20	D3	-2.20	0.02 2	2.83	-9.21	219	42	220	5.27	401	5.20	95.66	8.02	1.38	0.73	4.46	2.15	0.81
ZK-1-20 2	28.90	D3	-2.17	0.04 2	2.89	-9.22	209	47	226	4.82	590	9.57	53.95	4.90	2.40	0.83	5.77	1.96	0.59
ZK-1-21 2	9.90	D3	-2.15	0.04 2	2.80	-9.67	231	62	227	3.69	675	6.40	45.80	9.62	2.36	1.04	6.08	2.01	0.67
ZK-1-22 3	30.20	D1	-2.28	0.01 1	1.02	-10.72	141	31	145	4.69	494	5.14	23.91	6.00	1.72	0.84	4.82	2.06	0.64
ZK-1-23 3	30.70	D1	-2.18	0.02 2	2.87	-8.05	237	36	124	3.44	587	7.46	111.60	4.82	2.09	0.73	5.11	2.24	0.63
ZK-1-24 3	31.20	D3	-2.21	0.04 2	2.45	-9.92	188	59	216	3.64	487	15.59	75.26	3.81	1.14	0.84	3.83	2.09	0.73
ZK-1-25 3	31.40	D2	-2.20	0.03 2	2.65	-7.82	222	41	95	2.29	595	6.90	82.24	6.01	1.63	0.63	4.52	1.66	0.71
ZK-1-26 3	31.60	D3	-2.16	0.03 2	2.72	-10.14	236	118	178	1.51	470	16.03	87.01	7.35	2.81	0.90	2.91	1.34	0.78
ZK-1-27 3	32.00	D1	-2.17	0.02 2	2.87	-9.20	223	30	173	5.76	416	6.82	75.76	4.41	2.04	0.71	4.69	2.44	0.52
ZK-1-28 3	32.20	D1	-2.23	0.04 2	2.70	-8.09	247	39	112	2.83	522	9.25	79.74	4.25	2.27	1.30	7.64	3.45	0.76
ZK-1-29 3	32.70	D1	-2.25	0.03 2	2.26	-10.32	199	41	141	3.41	560	4.81	35.73	8.61	2.38	0.52	3.65	1.48	0.66
ZK-1-30 3	3.10	D1	-2.27	0.04 1	1.90	-9.77	234	33	141	4.32	1748	2.46	31.27	13.25	1.04	0.67	3.86	1.63	0.76
ZK-1-31 3	3.65	D2	-2.26	0.02 1	1.95	-9.68	216	32	145	4.49	505	3.07	36.04	10.47	0.93	0.98	5.96	2.86	0.71
ZK-1-32 3	34.15	D2	-2.28	0.04 1	1.64	-10.61	196	30	196	6.53	642	3.22	31.09	9.33	0.96	0.56	3.83	1.81	0.58
ZK-1-33 3	34.40	D2	-2.25	0.03 1	1.81	-10.24	250	28	225	7.99	540	4.84	27.46	5.82	1.16	0.74	4.54	2.36	0.46
ZK-1-34 3	34.80	D3	-2.22	0.05 1	1.98	-9.92	264	30	204	6.77	547	11.89	45.47	2.54	1.57	0.58	3.90	1.69	0.83
ZK-1-35 3	35.50	D2	-2.27	0.02 1	1.29	-10.23	201	36	117	3.24	473	2.64	7.90	13.76	1.34	0.64	4.91	1.96	0.64
ZK-1-36 3	86.05	D2	-2.19	0.04 2	2.69	-9.22	227	32	180	5.58	368	5.93	86.71	5.43	1.12	0.60	4.01	1.84	0.69
ZK-1-37 3	86.65	D2	-2.23	0.03 2	2.08	-9.59	210	37	135	3.68	449	3.11	45.67	11.82	0.95	0.51	3.90	1.36	0.78
ZK-1-38 3	37.00	D2	-2.16	0.03 2	2.75	-7.95	216	33	87	2.64	606	2.00	47.72	16.41	1.59	0.62	3.65	1.39	0.57
ZK-1-39 3	37.40	D1	-2.15	0.02 2	2.84	-7.81	217	31	71	2.32	425	3.08	104.08	10.03	1.98	0.86	4.53	1.82	0.55
ZK-1-40 3	37.95	D1	-2.21	0.04 1	1.66	-9.85	188	27	87	3.18	735	4.57	37.47	5.98	1.57	0.61	4.66	2.55	0.75
JDO-1 -	-	-	-2.34	0.05 -	-	_	-	_	_	-	-	-	-	-	-	-	_	_	_

 δ Eu values range from 0.23 to 1.14 (Fig. 3(d)). The summation of rare earth elements (ΣREE) range from 0.51 to 1.43 ppm, and the ratio of light rare earth elements to heavy rare earth elements (LREE/HREE) spans from 2.91 to 9.31 (Fig. 3(e)). Remarkably, the Na content, Mn/Sr ratio, Fe content, Ba content, δCe, and δEu exhibit similarities among the three matrix dolostones. Furthermore, the dolostones exhibit similar patterns of rare earth element distribution to the contemporaneous limestone, as shown in Fig. 3(f).

The δ^{26} Mg values range from -2.28% to -2.04%, the δ^{13} C values range from 1.02% to 2.95%, and the δ^{18} O values range from -10.72% to -7.81%. No significant differences in the Mg-C-O isotope compositions were observed among D1, D2, and D3 (Fig. 4). There is no discernible correlation between the δ^{26} Mg values and δ^{18} O values in all dolostone samples (Fig. 4(a)). However, a correlation is evident between the δ^{26} Mg values and δ^{13} C values (Fig. 4(b)). The δ^{26} Mg values do not exhibit a systematic increasing or decreasing trend with increasing Mn/Sr and δ Eu values (Fig. 4(c), (d)).

5. Discussion

5.1. Formation time and diagenetic sequence of dolostone

The petrological characteristics of dolostone, such as lithological composition, sedimentary structures, pore types, crystal

morphology, and crystal size, provide direct evidence for determining its formation time and diagenetic sequence (Jiang et al., 2022). In the Geluguanna profile, there is an alternating development of dolostone and limestone, both containing similar bioclastic components (Fig. 2(a), (b)). Microscopic examinations indicate the presence of residual granular structures originating from grainstone precursors in nearly all dolostone samples (Fig. 2(c)–(k)). These petrological features, closely associated with limestone, imply that the dolostone in the Buqu Formation is of secondary diagenetic origin rather than primary precipitation (Haas et al., 2014).

Under conditions where temperatures are below 50 °C, dolomite primarily grows with planar crystal faces, while the proportion of non-planar crystal faces increases when the temperature exceeds 50 °C (Gregg and Sibley, 1984). D1 mainly exhibits planar crystal faces, appearing as euhedral or subhedral forms (Fig. 2(c), (d)), suggesting that the formation temperature of D1 likely remained below 50 °C. D1 develops leached pores and sparry calcite cements (Fig. 2(c), (d)). The leached pores are formed by calcite cements in the early stage of atmospheric freshwater dissolution, while the sparry calcite cements are usually formed by reprecipitation of minerals in atmospheric precipitation or groundwater in the supergene environment. Considering the robust resistance to compaction of dolostone, early-formed dolostone can provide a stable framework for preserving epidiagenetic

Table 2Analysis data of rare earth elements in the dolostone of the Buqu Formation of the Middle Jurassic.

Number	Depth, m	Lithology	La ppm	Co. ppm	Dr. ppm	Nd ppm	Cm nnm	Eu ppm	Cd ppm	Th nnm	Dv. ppm	Uo ppm	Er ppm	Tm. nnm	Vh. nnm	Lu ppm
ZK-1-1	20.10	D2	0.137	0.583	0.059	0.177	0.025	0.003	0.032	0.005	0.030	0.007	0.024	0.003	0.026	0.004
ZK-1-2	20.50	D2	0.155	0.707	0.058	0.130	0.075	0.004	0.034	0.003	0.032	0.007	0.028	0.003	0.028	0.005
ZK-1-3	20.85	D1	0.084	0.345	0.038	0.149	0.028	0.010	0.033	0.005	0.030	0.008	0.026	0.004	0.029	0.005
ZK-1-4	21.50	D2	0.169	0.598	0.063	0.210	0.030	0.004	0.031	0.005	0.029	0.008	0.023	0.004	0.028	0.006
ZK-1-5	22.00	D2	0.117	0.362	0.046	0.156	0.028	0.004	0.028	0.004	0.030	0.008	0.025	0.004	0.028	0.005
ZK-1-6	22.40	D1	0.086	0.389	0.021	0.074	0.017	0.007	0.019	0.004	0.028	0.007	0.024	0.004	0.027	0.005
ZK-1-7	23.00	D3	0.123	0.538	0.025	0.093	0.020	0.005	0.027	0.004	0.028	0.008	0.023	0.004	0.025	0.004
ZK-1-8	23.85	D2	0.139	0.436	0.026	0.098	0.021	0.006	0.030	0.005	0.033	0.009	0.028	0.006	0.035	0.006
ZK-1-9	24.25	D2	0.101	0.615	0.021	0.091	0.018	0.005	0.026	0.005	0.039	0.009	0.033	0.006	0.036	0.007
ZK-1-10		D2	0.110	0.491	0.021	0.093	0.022	0.006	0.024	0.005	0.028	0.008	0.027	0.005	0.031	0.006
ZK-1-11		D1	0.117	0.361	0.020	0.090	0.018	0.006	0.023	0.003	0.027	0.008	0.023	0.004	0.031	0.005
ZK-1-12		D3	0.145 0.088	0.528	0.024	0.088	0.020	0.005	0.025	0.004	0.029	0.007 0.008	0.025	0.004	0.031	0.006
ZK-1-13		D3		0.375	0.017	0.095	0.018	0.005	0.025	0.004	0.030		0.028	0.004	0.032	0.005
ZK-1-14		D1	0.117	0.422	0.029	0.141	0.022	0.005	0.025 0.027	0.004	0.029	0.007	0.025	0.004	0.030	0.005
ZK-1-15		D1	0.090	0.404	0.023	0.081	0.023	0.006		0.004	0.030	0.007	0.023	0.004	0.026	0.005
ZK-1-16		D1	0.090	0.208	0.023	0.097	0.021	0.004	0.025	0.004	0.029	0.007	0.024	0.004	0.025	0.005
ZK-1-17		D1	0.211	0.678	0.071	0.231	0.033	0.008	0.034	0.004	0.033	0.008	0.024	0.003	0.024	0.005
ZK-1-18		D1	0.087	0.301	0.020	0.079	0.020	0.004	0.020	0.004	0.027	0.007	0.025	0.004	0.025	0.005
ZK-1-19		D3 D3	0.095	0.395	0.019	0.071	0.014	0.005	0.023	0.004	0.032	0.007 0.007	0.025	0.005	0.033	0.006
ZK-1-20			0.115	0.446 0.575	0.025 0.031	0.096	0.020	0.004	0.025 0.031	0.004	0.029	0.007	0.023 0.027	0.004	0.025	0.005 0.006
ZK-1-21		D3	0.144			0.115	0.024			0.005	0.033			0.005	0.031	
ZK-1-22		D1	0.081	0.338	0.018	0.237	0.016	0.004	0.023	0.004	0.027	0.007	0.046	0.004	0.028	0.005
ZK-1-23		D1	0.090	0.398	0.019	0.078	0.020	0.004	0.023	0.004	0.029	0.007	0.022	0.004	0.026	0.005
ZK-1-24		D3	0.101	0.424	0.023	0.088	0.021	0.006	0.034	0.006	0.045	0.011	0.032	0.005	0.035	0.006
ZK-1-25		D2	0.097	0.309	0.019	0.071	0.016	0.004	0.022	0.004	0.025	0.006	0.022	0.003	0.026	0.005
ZK-1-26 ZK-1-27		D3 D1	0.128 0.071	0.351 0.367	0.030 0.018	0.130 0.107	0.022 0.021	0.008 0.004	0.040 0.021	0.008 0.004	0.051 0.029	0.014	0.046 0.027	0.008 0.004	0.052 0.027	0.010 0.006
ZK-1-28 ZK-1-29		D1 D1	0.126 0.076	0.795 0.225	0.021 0.017	0.180 0.070	0.018	0.006 0.005	0.029 0.023	0.005 0.004	0.031 0.028	0.008	0.037 0.022	0.004 0.003	0.031 0.021	0.005 0.005
ZK-1-29 ZK-1-30		DI D1	0.076	0.225	0.017	0.070	0.019 0.018	0.005	0.023	0.004	0.028	0.006	0.022	0.003	0.021	0.005
								0.005	0.023		0.033	0.008	0.027		0.032	
ZK-1-31 ZK-1-32		D2 D2	0.101 0.074	0.565 0.271	0.021 0.017	0.132 0.058	0.016 0.018	0.003	0.025	0.004 0.004	0.031	0.007	0.032	0.004 0.004	0.033	0.005 0.005
ZK-1-32 ZK-1-33		D2 D2	0.074	0.271	0.017	0.058	0.018	0.003	0.018	0.004	0.027	0.007	0.022	0.004	0.028	0.005
ZK-1-33 ZK-1-34		D2 D3	0.079	0.376	0.018	0.110		0.003	0.025	0.004	0.026	0.007	0.031	0.004		0.005
ZK-1-34 ZK-1-35		D3 D2	0.080	0.271	0.018	0.072	0.016 0.015	0.003	0.020	0.004	0.026	0.007	0.023	0.004	0.030 0.027	0.005
ZK-1-35 ZK-1-36		D2 D2	0.089	0.335	0.017	0.073	0.015	0.003	0.017	0.003	0.023	0.006	0.024	0.004	0.027	0.005
ZK-1-36 ZK-1-37		D2 D2	0.084	0.294	0.016	0.064	0.015	0.004	0.020	0.003	0.026	0.007	0.025	0.005	0.027	0.005
ZK-1-37 ZK-1-38		D2 D2	0.087	0.221	0.016	0.083	0.014	0.004	0.020	0.003	0.023	0.008	0.021	0.004	0.023	0.004
ZK-1-38 ZK-1-39		D2 D1	0.093	0.264	0.021	0.083	0.019	0.004	0.024	0.004	0.029	0.008	0.028	0.004	0.030	0.006
ZK-1-39 ZK-1-40		D1 D1	0.075	0.287	0.019	0.304	0.018	0.004	0.031	0.005	0.025	0.007	0.048	0.004	0.031	0.006
ZK-1-40	57.95	וע	0.007	U.333	0.010	0.054	0.012	0.004	0.019	0.004	0.023	0.007	0.023	0.003	0.025	0.005

pores or freshwater cements (Zhao et al., 2018). These preserved freshwater cements and leached pores indicate that D1 was formed by epidiagenetic dolomitization in the early diagenesis stage (Shen et al., 2019). The CL image of D1 shows that the center of most dolomite crystals is darker and the edge is brighter, which exhibits certain degree of buried dolomite characteristics (Fig. 2(e)). The burial history curve of the Middle Jurassic Bugu Formation in the South Plateau Depression indicates that the deepest burial depth of the Bugu Formation is approximately 4000 m (Wu et al., 2020). Assuming a surface temperature of 25 °C and a geothermal gradient of 26.6 °C/km, the corresponding formation temperature of the Buqu Formation at a burial depth of 4000 m is estimated to be around 131.4 °C (Fig. 5). Consequently, D1 has undergone deep burial compaction and high temperatures. These conditions likely led to the superimposition of burial-adjusted dolomitization on D1, causing it to dissolve-recrystallize and exhibit darker center and brighter edge CL characteristics.

The residual oolites of D2 and the leached moldic pores (Fig. 2(f), (g)) suggest a close association of D2 with early meteoric diagenesis. Previous research has indicated that when a mineral's crystal radius reaches or surpasses its critical crystal radius, the crystal will continue to grow, forming larger crystals (Gregg et al., 1992). In comparison to D1, D2 displays larger dolomite crystals (Fig. 2(f), (g)), a more frequent non-planar crystal surface, and stronger cathodoluminescence (Fig. 2(h)), indicating a later and deeper formation of D2 relative to D1. The dolomite crystals in D3 are

characterized by the largest size (Fig. 2(i), (j)) and the strongest cathodoluminescence (Fig. 2(k)), suggesting that the formation of D3 required an extended period and likely involved additional recrystallization processes based on D2.

The analysis of diagenesis sequence reveals that D1 originated from the dolomitization of grainstone in the early diagenetic phase, whereas D2 and D3 resulted from the recrystallization of D1 during the later burial phase.

5.2. Tracing the source of dolomitization fluids

5.2.1. Assessing the reliability of geochemical data

The dolostone samples examined research exhibit a predominant dark red CL signature (Fig. 2(e), (h), (k)). The Mn/Sr ratios generally do not exceed 8 (Fig. 3(a)), and there is a minimal correlation between Fe and Mn content (Fig. 3(b)), suggesting a relatively mild burial diagenesis and associated alteration processes (Jacobsen and Kaufman, 1999; Li et al., 2019). Additionally, the concentration of Ba in these samples remains below 25 ppm, and the δ Eu values consistently register below 1 (Fig. 3(c)), indicating a limited impact of high-temperature hydrothermal fluids on these samples (Chakhmouradian et al., 2016; Hu et al., 2019). The Σ REE concentration in the analyzed samples is notably lower compared to that observed in terrigenous sediments, suggesting a minor impact of terrigenous components has little effect (Benabdelkader et al., 2019) (Fig. 3(e)).

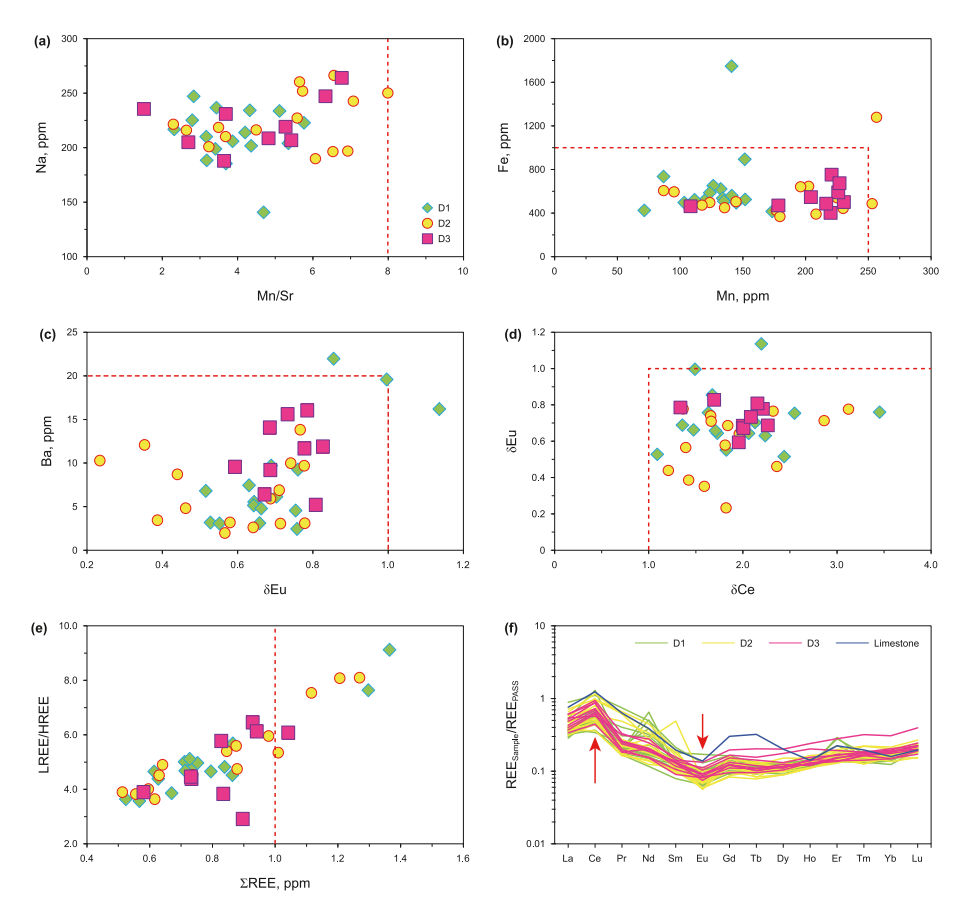


Fig. 3. Element interaction diagram of dolostone. (a) Na content vs. Mn/Sr; (b) Fe content vs. Mn content; (c) Ba content vs. δEu values; (d) δEu values vs. δCe values; (e) HREE/LREE vs. ΣREE; (f) REE distribution pattern diagram of dolostones and limestone.

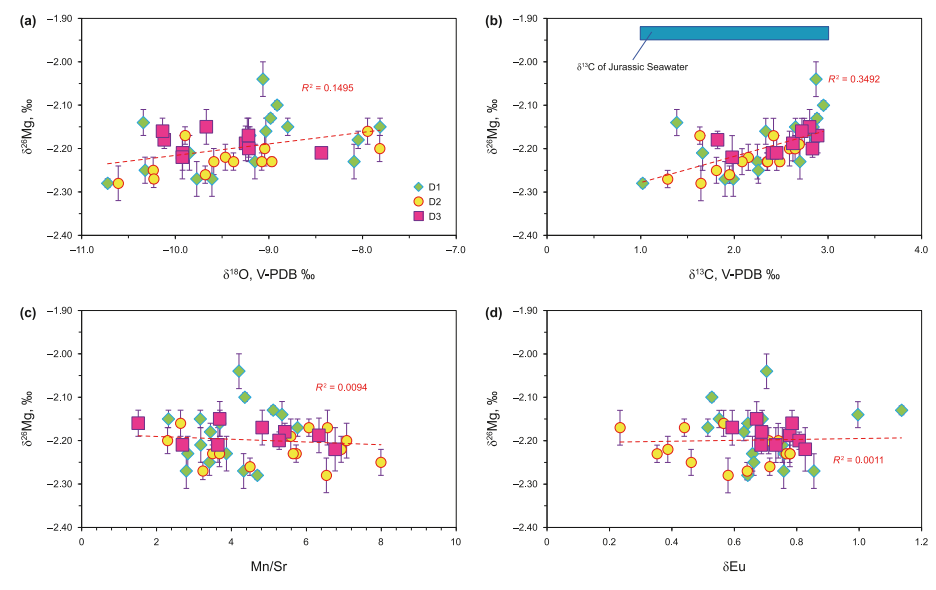


Fig. 4. Mg-C-O-isotopes interaction diagram of dolostone. (a) δ^{26} Mg values vs. δ^{18} O values; (b) δ^{26} Mg values vs. δ^{13} C values; (c) δ^{26} Mg values vs. Mn/Sr; (d) δ^{26} Mg values vs. δ^{18} O values; (b) δ^{26} Mg values vs. δ^{18} O values; (c) δ^{26} Mg values vs. δ^{18} O values; (d) δ^{26} Mg values vs. δ^{18} O values; (e) δ^{26} Mg values vs. δ^{18} O values; (e) δ^{26} Mg values vs. δ^{18} O values; (e) δ^{26} Mg values vs. δ^{18} O values; (f) δ^{26} Mg values vs. δ^{18} O values; (g) δ^{26} Mg values vs. δ^{18} O values; (h) δ^{26} Mg values vs. δ^{18} O values vs.

The susceptibility of oxygen isotopes to temperature variations often leads to a decrease in δ^{18} O values of dolostones during burial heating (Al-Aasm, 2000). The δ^{18} O values of the dolostone samples consistently fall below -5%, with their significant negative deviation potentially reflecting alterations in the oxygen isotopic

composition due to elevated temperatures (Fig. 4(a)). The range in δ^{13} C values among the samples is limited, indicating a minor influence of burial diagenesis on carbon isotopes (Fig. 4(b)). Mg isotopes of dolostones are typically resistant to diagenetic alterations (Geske et al., 2012; Hu et al., 2017; Qing et al., 2023). Despite the

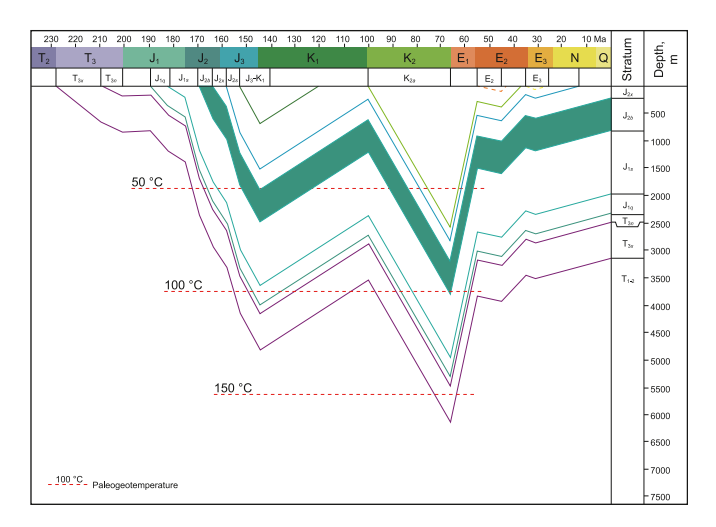


Fig. 5. Burial-thermal evolution history of the Middle Jurassic Buqu Formation (Wu et al., 2020). Description: T_{3x} —Upper Triassic Xiaochaka Formation, T_{3n} —Upper Triassic Nadigangri Formation, J_{1q} —Lower Jurassic Quse Formation, J_{1s} —Lower Jurassic Sewa Formation, J_{2b} —Middle Jurassic Buqu Formation, J_{2x} —Middle Jurassic Xiali Formation, J_{2s} — Middle Jurassic Suowa Formation.

recrystallization of dolomite crystals, the δ^{26} Mg values remain stable (Ning et al., 2019). The δ^{26} Mg values for the D1, D2, and D3 dolostones in the Buqu Formation display minimal difference and do not show correlations with δ^{18} O, Mn/Sr, or δ Eu values, indicating the preservation of the Mg isotopic composition through subsequent diagenetic processes (Fig. 4(a), (c), (d)).

The comprehensive evaluation of geochemical data suggests that the δ^{13} O has undergone a negative bias due to the influence of high burial temperature in the strata, but the element content, δ^{13} C and δ^{26} Mg reflect the original geochemical signals.

5.2.2. Source of dolomitization fluid

Dolomitization primarily involves the replacement of Ca²⁺ ions in limestone with Mg²⁺ ions in the fluid, leading to the transformation of limestone into dolostone (Machel, 2004; Gomez-Rivas et al., 2014; Centrella et al., 2023). The fluids responsible for this alteration process encompass a variety of types, such as mixed water (freshwater and seawater), hydrothermal fluids, burial formation water, seawater, and pore water. Upon interaction with these diverse fluid compositions, the resulting dolostones display distinct elemental and isotopic geochemical properties (Kretz, 1982; Lin et al., 2022).

Mixed water refers to a fluid amalgamation of meteoric water and seawater (Badiozamani, 1973). Dolostones that form through interactions with mixed water typically exhibit low Na content, high Mn content, and negative δ^{13} C values (Haeri-Ardakani et al., 2013; Li et al., 2013). However, the dolostone samples from the Bugu Formation show high Na content (Fig. 3(a)), low Mn content (Fig. 3(b)), and positive δ^{13} C values (Fig. 4(b)). These characteristics deviate from the usual elemental and isotopic traits associated with dolomitization by mixed water. Additionally, typical hydrothermal minerals produced by hydrothermal processes, such as sphalerite, galena, and quartz, were not detected in any of the dolostone samples (Davies and Smith, 2006) (Fig. 2). Furthermore, these samples lack the high Ba content and positive δEu anomaly that are indicative of hydrothermal dolostones (Chakhmouradian et al., 2016) (Fig. 3(c)). The absence of a thick mud shale layer above the dolostone in the Buqu Formation also diminishes the likelihood of dolomitization fluids originating from the formation brine released by the overlying mud shale (Fig. 1(c)).

Mass balance calculations indicate that a high water-to-rock

ratio is a crucial prerequisite for the formation of large-scale dolostones (Sena et al., 2014). The dolostones of the Bugu Formation, spanning thousands of square kilometers and attaining thicknesses of hundreds of meters within the Southern Plateau Basin (Fig. 1(b)). The formation of substantial dolomite layers in the Buqu Formation is primarily attributed to seawater acting as the principal fluid source. This is supported by the hydrogeological characteristics of seawater, which can supply the necessary high water to rock ratio conducive to large-scale dolomitization (Warren, 2000). Seawater maintains a relatively stable Mg isotope composition, leading to dolostones formed in seawater often displaying consistent δ^{26} Mg values (Geske et al., 2012, 2015). This study reveals a maximal difference of 0.24‰ in $\delta^{26}\text{Mg}$ values among the dolostone samples (Fig. 4(b)). Additionally, these dolostone samples exhibit a carbon isotope composition closely resembling that of Middle Jurassic seawater (Veizer et al., 1999) (Fig. 4(b)). The stable δ^{26} Mg and δ^{13} C values offer compelling evidence that the fluids responsible for the early dolostone formation in the Buqu Formation originated from seawater during the same

The distribution patterns of REE in marine authigenic carbonates and seawater typically exhibit negative Ce anomalies and depleted LREE (Tostevin et al., 2016). However, the elemental analysis of the Bugu Formation dolostones reveals positive δCe values (Fig. 3(d)) and enriched LREE contents (Fig. 3(e), (f)), which deviate significantly from the expected composition of marine authigenic carbonates and seawater. In oxidizing environments, the soluble Ce³⁺ present in sedimentary water is readily oxidized by dissolved oxygen, leading to the formation of insoluble and immobile Ce⁴⁺ that adsorb onto sediment particles' surfaces. This process results in a notable positive Ce anomaly in the sediment, while a negative Ce anomaly is observed in the fluid phase saturating the sediment (Nothdurft et al., 2004). The dolostones from the Buqu Formation exhibit a distinct positive Ce anomaly, contrasting with the negative Ce anomaly typically found in seawater, indicating a dynamic equilibrium of Ce between seawater and carbonate sediments. This suggests that the diagenetic fluid responsible for the dolostone formation is oxidized seawater. Likewise, the LREE in the oxidized seawater are readily scavenged, leading to the observed LREE enrichment characteristics in the dolostones.

Dolostones formed through reactions with burial pore water commonly exhibit enrichment of Fe and Mn elements, with Fe and Mn contents typically surpassing 1000 and 250 ppm, respectively (Budd, 1997; Wei et al., 2023). However, the dolostone samples collected in this study generally exhibit Fe contents below 1000 ppm and Mn contents lower than 250 ppm (Fig. 3(b)). This suggests that the burial pore water may not be the primary factor in dolomitization (Zenger, 1983). It is important to highlight that as crystal size increases (D1 \rightarrow D2 \rightarrow D3), the Mn content of dolostone gradually increases (Fig. 3(b)), indicating the influence of late buried pore water on dolostone. At the same time, the late burial adjustment dolomitization significantly impacted the δ^{18} O value of dolostone, leading to a notable negative bias (Fig. 4(a)).

Based on the comprehensive elements and C-O-Mg isotopes, the early dolomitization fluid of the Buqu Formation dolostone is oxidized seawater, while the late dolomitization fluid is buried pore water.

5.3. Coupling mechanism between sea level changes and Mg isotope

Previous research has suggested that massive dolostone deposits is attributed to the continuous superposition of periodic dolomitization processes related to sea-level fluctuations

(Lumsden, 1988). Since the Late Triassic, with the gradual opening of the Bangong Lake-Nujiang Ocean Basin, the evolutionary history of the Mesozoic Jurassic marine basin began, and seawater gradually invaded from south to north. During the Early Jurassic to Late Jurassic period, the relative sea level in the Plateau Basin demonstrated a general upward trajectory (Hallam, 2001). This basin experienced a significant transgression event during the sedimentary period of the Bugu Formation in the Middle Jurassic. which resulted in the widespread coverage of the basin by seawater (Xue et al., 2020) (Fig. 6). The continuously rising sea level promoted the expansion of carbonate platforms, potentially creating favorable conditions for limestone sedimentation and subsequent widespread dolomitization (Hu et al., 2024). In the Geluguanna section, alternating occurrences of limestone and dolostone can be observed, with limestone developed in the deeper water phase, and dolostone forming during shallower water phases (Fig. 2(a)). This observation leads us to speculate that sea level fluctuations likely played a pivotal role in governing the formation and distribution of dolostones within the Buqu Formation.

The deduction of sea level fluctuations can be indirectly inferred through the analysis of vertical variations in lithology, isotope composition, and element content (Natalicchio et al., 2019). As sealevel drops, the Na content of carbonate rocks tends to increase, while the ratios of Sr/Cu, Sr/Ba, Rb/Sr, and Σ REE show a decline (Langmuir and Melchior, 1985; Nicholls, 1967; Stoll and Schrag, 2001). The examination of dolostone samples from Well ZK-1 reveals higher Na content and lower Sr/Cu, Sr/Ba, Rb/Sr, and Σ REE levels, indicating a shallow water environment during dolomitization. This finding aligns with the sedimentary conditions of an inner platform shoal (Fig. 7). Previous studies have also confirmed

that this sedimentary environment within inner platform shoals is conducive to dolomitization, as seen in examples such as the dolostones in the Early Cambrian Xiaoerbulak Formation in the Tarim Basin (Zhu et al., 2023) and the Early Cambrian Longwangmiao Formation in the Sichuan Basin (Wang et al., 2021). Additionally, $\delta^{13}C$ values in marine carbonates are positively correlated with sea level fluctuations (Jarvis et al., 2001, 2002; Hu et al., 2024). The consistent vertical trends in $\delta^{13}C$, Na, Sr/Cu, Sr/Ba, Rb/Sr, and Σ REE of the dolostones from Well ZK-1 suggest fluctuations in sea level rise (Fig. 7).

Statistical analyses of the Mg isotope compositions in published studies of dolostones and limestones have revealed that the δ^{26} Mg values of dolostones generally exceed those of limestones by approximately 2% (Teng, 2017). This observation suggests that δ^{26} Mg will be gradually enriched during the fluid migration process of dolomitization (Huang et al., 2015; Bialik et al., 2018; Li et al., 2022, 2023). Analysis of dolostone samples from Well ZK-1 has identified four similar sequences where $\delta^{26}Mg$ values exhibit an initial decrease followed by an increase, accompanied by a rise in sea level followed by a decline (Fig. 7). Specifically, a rise in sea level brings open seawater with lower δ^{26} Mg values into confined water bodies. The influx of seawater into the carbonate platform initiates dolomitization in the underlying limestone, leading to a decline in the δ^{26} Mg values of dolostones (Fig. 8(a)). Conversely, a decrease in sea level prompts evaporated seawater from restricted environments to migrate upwards through capillary action into overlying limestone sediments. As dolomitization advances, the consumption of ²⁴Mg leads to an enrichment of the remaining seawater in ²⁶Mg. ultimately causing an increase in the δ^{26} Mg values of dolostones (Fig. 8(b)). The significant correlation between sea level

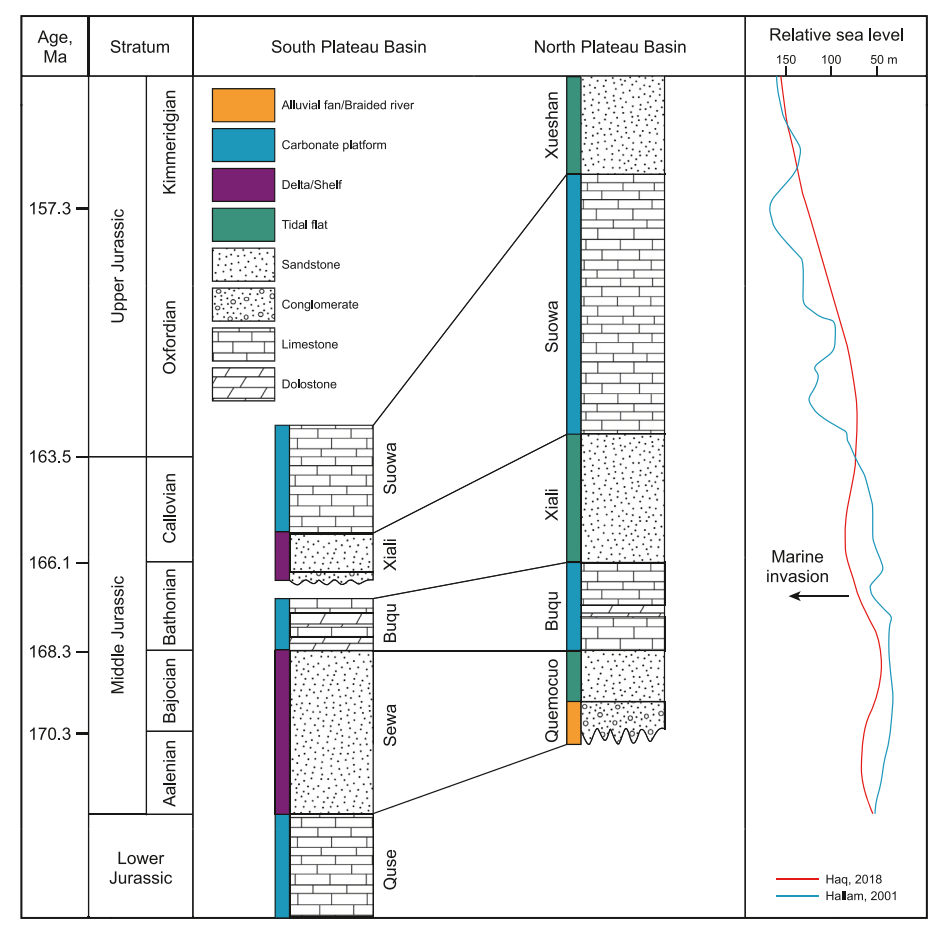


Fig. 6. Jurassic stratigraphic lithology, sedimentary environment, and sea level changes (Xue et al., 2020).

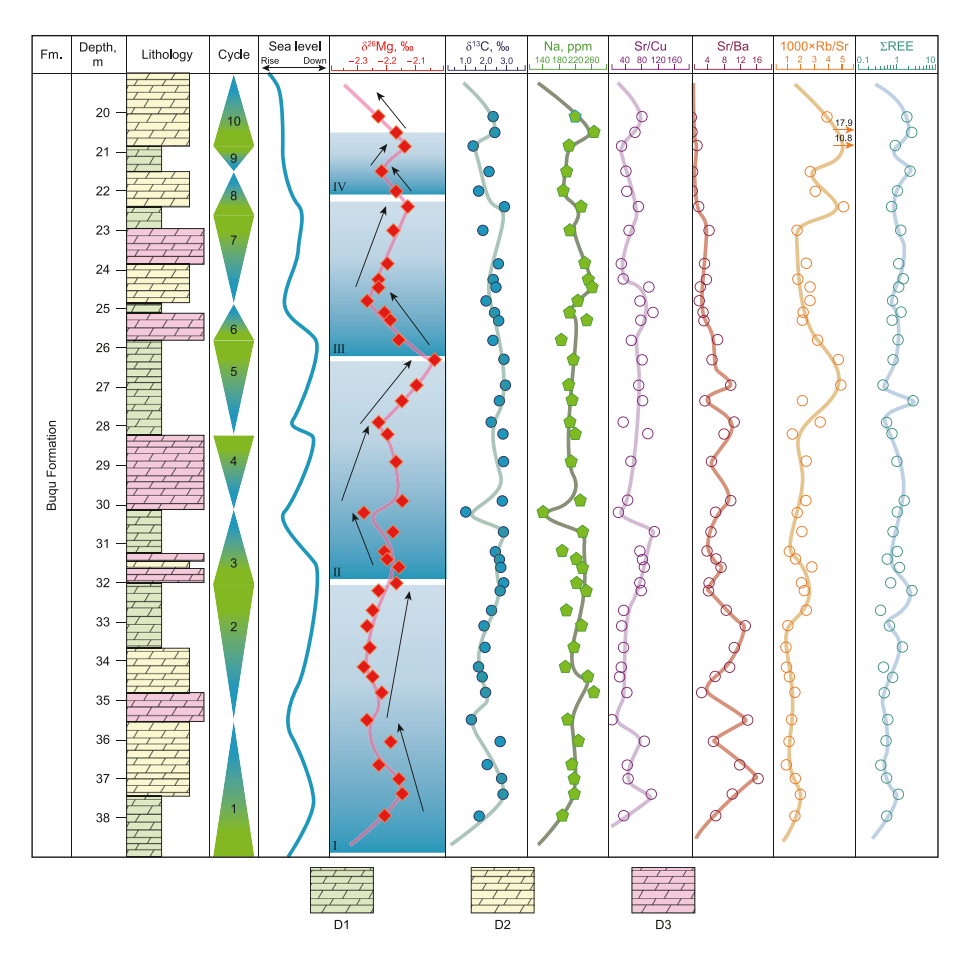


Fig. 7. Dolostone sampling section of Well ZK-1, displaying the vertical variation of Mg-C isotope composition, element content, and relative sea level.

fluctuations and Mg isotopes in dolostones from Well ZK-1 confirms the pivotal role of sea level changes in governing the formation and distribution of dolostones in the Buqu Formation.

5.4. Genetic mechanism of Buqu formation dolostone

Based on the aforementioned research on the diagenetic sequence, fluid sources of dolomitization, and sea level changes of the Buqu Formation dolostone, combined with the tectonic lith-ofacies paleogeographic background, this study has formulated a model for the formation and evolution of the Buqu Formation

dolostone. The dolostone formation in the Buqu Formation has undergone the processes of limestone sedimentation, early seawater dolomitization, and late burial adjustment dolomitization (Fig. 9).

Limestone sedimentation stage. With the expansion of the Bangong Lake-Nujiang Ocean expanded, seawater gradually infiltrated from the south to the north. This occurred during the sedimentary period of the Middle Jurassic Buqu Formation, leading to the submergence of most carbonate platforms by water bodies. The grainstone deposited in the higher regions of the platform is susceptible to developing leached pores, moldic pores, and freshwater

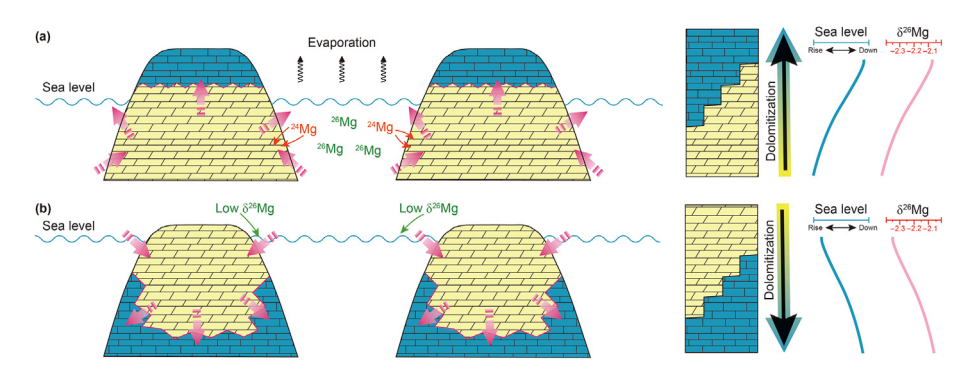


Fig. 8. Response pattern of Mg isotope to sea level changes and dolomitization fluid migration. **(a)** When the sea level drops, the evaporation of seawater in a confined environment leads to dolomitization moving upward through capillary action, and the δ^{26} Mg value shows an upward trend. **(b)** When the sea level rises, seawater with a low δ^{26} Mg value intrudes into the platform, seeping downward and causing dolomitization. As a result, the δ^{26} Mg value exhibits a decreasing trend upwards.

cements, influenced by atmospheric freshwater exposure above sea level. Conversely, the micrite limestone deposited in the lower part of the platform usually exhibits low porosity due to prolonged exposure to sea level (Fig. 9(a)).

Early stage of seawater dolomitization stage. Previous research has identified various combinations of evaporite-limestonedolostone in the Middle Iurassic Bugu Formation through on-site outcrop observation and examination of thin sections (Yang et al., 2017). Combined with the paleogeographic background, it is evident that the Plateau Basin was situated in a low-latitude region north of the equator during the sedimentation of the Bugu Formation, characterized by a hot, semi-arid, and semi-humid paleoclimate (Ma et al., 2023). This paleoclimate, along with the fluctuating sea levels, created favorable conditions for dolomitization. As the sea level rose and reached a highstand, evaporated seawater inundating the platform percolated downward through the pores under gravitational influence, leading to the conversion of previously deposited grainstone in the elevated areas of the platform into granular dolostone. Subsequently, as the sea level fell, transitioning into a lowstand, the sedimentary setting shifted from an open platform to a restricted platform. The absence of prompt seawater replenishment from the Bangong Lake-Nujiang Ocean, coupled with evaporation, resulted in the salinization of the water body, prompting the transformation of the previously deposited micrite limestone in the lower part of the ancient topography into micrite dolostone. The recurrent fluctuations in sea level facilitated

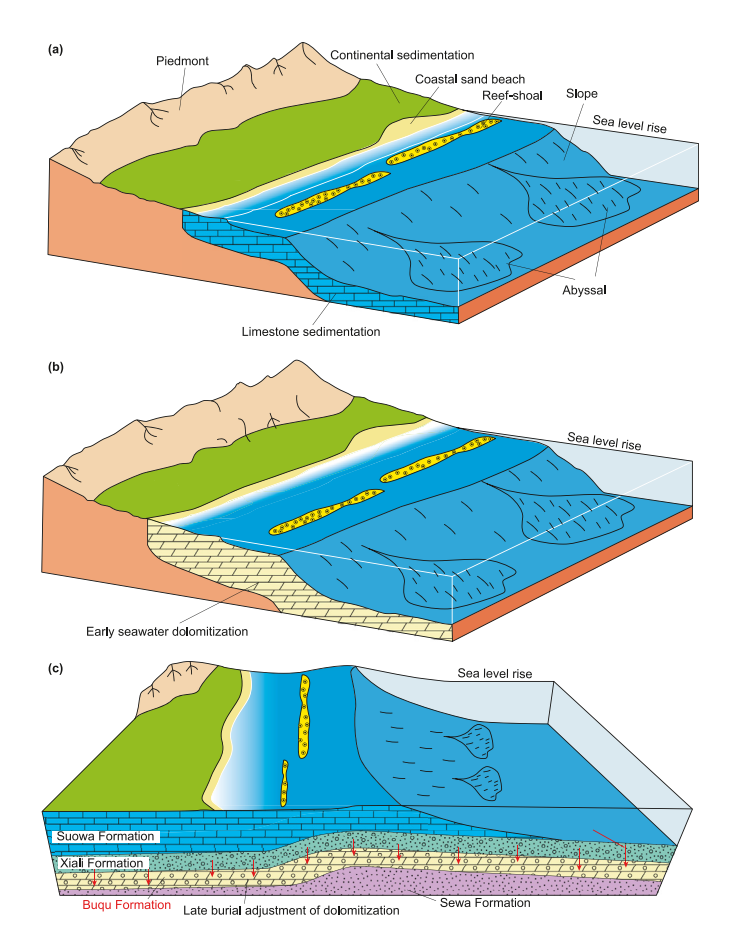


Fig. 9. Formation and evolution model of dolomite in Buqu Formation. **(a)** Limestone sedimentation stage; **(b)** Early seawater dolomitization stage; **(c)** Late burial adjustment dolomitization stage.

the continuous conversion of limestone on carbonate platforms into dolostone, gradually accumulating over an extended period to form extensive thick dolostone deposits (Fig. 9(b)).

Late burial adjustment of dolomitization stage. As the sediment above thickens and the formation progresses into the burial stage, early dolostone undergoes further adjustment through burial dolomitization under the combined action of pore water, high temperature, and high pressure. The slow exchange rate between pore water and minerals within the formation, along with the restriction of pore space on dolomite crystals in the burial setting, leads to the gradual evolution of very finely to finely crystalline dolostone (D1) into finely to medium crystalline dolostone (D2) and medium to coarsely crystalline dolostone (D3) (Fig. 9(c)).

6. Conclusion

Three types of matrix dolostones were identified of the Buqu Formation, namely very finely to finely crystalline dolostone (D1), finely to medium crystalline dolostone (D2), and medium to coarsely crystalline dolostone (D3). D1 originated from the dolomitization of grainstone in the early diagenetic phase, whereas D2 and D3 resulted from the recrystallization of D1 during the later burial phase.

The presence of Na>100 ppm, Fe < 1000 ppm, Mn < 250 ppm, Ce positive anomaly, LREE enrichment, stable $\delta^{26} Mg$ value, and $\delta^{13} C$ value indicate that the early dolomitization fluid was oxidized seawater. As the crystal size increases (D1 \rightarrow D2 \rightarrow D3), the gradually increasing Mn and significantly negative biased $\delta^{18} O$ value indicate that the dolostone has undergone adjustment and transformation of buried pore water in the late stage.

The widespread Middle Jurassic transgression event in the Plateau Basin resulted in the continuous expansion of the carbonate platform, creating conducive conditions for the deposition of precursor limestone and extensive dolomitization. The sea level fluctuations during the sedimentary phase of the Buqu Formation were reconstructed by analyzing the consistent patterns of $\delta^{13} \text{C}$, Na, Sr/Cu, Sr/Ba, Rb/Sr, and \sum REE. The significant correlation between sea level and the $\delta^{26} \text{Mg}$ of dolostone confirms the pivotal role of sea level in governing the formation and distribution of early dolostone.

The formation of dolostone in the Buqu Formation involved two distinct stages: early seawater dolomitization and late burial dolomitization. Early seawater dolomitization was controlled by changes in sea level, and frequent sea level rise and fall led to the continuous transformation of limestone deposited on carbonate platforms into dolostone, which accumulated over a long period of time to form large-scale thick dolostone. Late burial adjustment of dolomitization is controlled by high Mg/Ca ratio pore water, high temperature, and high pressure. Early dolostone undergoes burial adjustment of dolomitization, causing mutual compression and growth of dolomite, finely crystalline, planar matrix dolostone (D1) is transformed into crystalline, non-planar dolostone (D2/D3).

The formation of dolostone in the Buqu Formation involved two distinct stages: early seawater dolomitization and late burial adjustment dolomitization. The early seawater dolomitization was controlled by fluctuations in sea level. The frequent rise and fall of sea levels resulted in the continuous transformation of limestone deposited on carbonate platforms into dolostone. This transformation occurred over an extended period, leading to the accumulation of thick dolostone.

The late burial adjustment of dolomitization is controlled by high Mg/Ca ratio pore water, high temperature, and high pressure. Early dolostone underwent adjustments due to burial, resulting in the compression and growth of dolomite crystals. The finely crystalline, planar dolostone (D1) is transformed into crystalline, non-

planar dolostone (D2/D3).

CRediT authorship contribution statement

Xi Li: Writing — original draft, Supervision, Methodology, Investigation, Data curation, Conceptualization. **An-Jiang Shen:** Writing — original draft, Supervision, Resources, Methodology, Investigation, Data curation, Conceptualization. **Rui-Lin Hao:** Methodology, Investigation, Data curation.

Conflict of interest

The authors declare that they have no known competing financial interests or personal relationships that could have appeared to influence the work reported in this paper.

References

- Adams, A., Diamond, L.W., Aschwanden, L., 2019. Dolomitization by hypersaline reflux into dense groundwaters as revealed by vertical trends in strontium and oxygen isotopes: upper Muschelkalk, Switzerland. Sedimentology 66 (1), 362–390. https://doi.org/10.1111/sed.12530.
- Al-Aasm, I.S., 2000. Chemical and isotopic constraints for recrystallization of sedimentary dolomites from the Western Canada Sedimentary Basin. Aquat. Geochem. 6, 227–248. https://doi.org/10.1023/A:1009611224589.
- Badiozamani, K., 1973. The dorag dolomitization model, application to the middle Ordovician of Wisconsin. J. Sediment. Res. 43, 965–984. https://doi.org/ 10.1306/74D728C9-2B21-11D7-8648000102C1865D.
- Baldwin, G.J., Thurston, P.C., Kamber, B.S., 2011. High-precision rare earth element, nickel, and chromium chemistry of chert microbands pre-screened with in-situ analysis. Chem. Geol. 285 (1–4), 133–143. https://doi.org/10.1016/j.chemgeo.2011.03.019.
- Bao, Z., Huang, K.J., Xu, J., Deng, L., Yang, S., Zhang, P., Yuan, H., 2020. Preparation and characterization of a new reference standard GSB-Mg for Mg isotopic analysis. J. Anal. Atomic Spectrom. 35 (6), 1080–1086. https://doi.org/10.1039/ D0IA00059K.
- Beinlich, A., Mavromatis, V., Austrheim, H., Oelkers, E.H., 2014. Inter-mineral Mg isotope fractionation during hydrothermal ultramafic rock alteration—Implications for the global Mg-cycle. Earth Planet Sci. Lett. 392 (1), 166—176. https://doi.org/10.1016/j.epsl.2014.02.028.
- Benabdelkader, A., Taleb, A., Probst, J.-L., Belaidi, N., Probst, A., 2019. Origin, distribution, and behaviour of rare earth elements in river bed sediments from a carbonate semi-arid basin (Tafna River, Algeria). Appl. Geochem. 106, 96–111. https://doi.org/10.1016/j.apgeochem.2019.05.005.
- Bi, D.J., Zhai, S.K., Zhang, D.J., Liu, X.F., Liu, X.Y., Jiang, L.J., Zhang, A.B., 2018. Constraints of fluid inclusions and C, O isotopic compositions on the origin of the dolomites in the Xisha Islands, South China Sea. Chem. Geol. 493, 504–517. https://doi.org/10.1016/j.chemgeo.2018.07.005.
- Bialik, O.M., Wang, X., Zhao, S., Waldmann, N.D., Frank, R., Li, W., 2018. Mg isotope response to dolomitization in hinterland-attached carbonate platforms: outlook of δ²⁶Mg as a tracer of basin restriction and seawater Mg/Ca ratio. Geochem. Cosmochim. Acta 235, 189–207. https://doi.org/10.1016/j.gca.2018.05.024.
- Budd, D.J., 1997. Cenozoic dolomites of carbonate islands: their attributes and origin. Earth Sci. Rev. 42 (1–2), 1–47. https://doi.org/10.1016/S0012-8252(96) 00051-7.
- Cai, W.K., Liu, J.H., Zhou, C.H., Keeling, J., Glasmacher, U.A., 2021. Structure, genesis and resources efficiency of dolomite: new insights and remaining enigmas. Chem. Geol. 573, 120191. https://doi.org/10.1016/j.chemgeo.2021.120191.
- Centrella, S., Hoareau, G., Beaudoin, N.E., Motte, G., Lanari, P., Piccoli, F., Callot, J.P., Gomez-Rivas, E., Martín-Martín, J.D., 2023. Estimating the fluid composition after dolomitization using mass balance equation: comparison of examples from Spain, Canada and France. Global Planet. Change 220, 104016. https://doi.org/10.1016/j.gloplacha.2022.104016.
- Chakhmouradian, A.R., Reguir, E.P., Couëslan, C., Yang, P., 2016. Calcite and dolomite in intrusive carbonatites. II. Trace-element variations. Mineral. Petrol. 110, 361–377. https://doi.org/10.1007/s00710-015-0392-4.
- Cheng, X., Wu, H.N., Diao, Z.B., Wang, H.J., Zhang, X.D., Ma, L., Zhou, Y.N., Kang, W.W., Ji, W.H., Li, R.S., 2012. New paleomagnetic result of the Middle-Late Jurassic rocks from northern Qiangtang Block, west China. Chin. J. Geophys. 55 (10), 3399–3409. https://doi.org/10.6038/j.issn.0001-5733.2012.10.023 (in Chinese).
- Clayton, R.N., Jones, B.F., 1968. Isotope studies of dolomite formation under sedimentary conditions. Geochem. Cosmochim. Acta 32 (4), 415–432. https://doi.org/10.1016/0016-7037(68)90076-8.
- Davies, G.R., Smith, L.B., 2006. Structurally controlled hydrothermal dolomite reservoir facies: an overview. AAPG Bull. 90 (11), 1641–1690. https://doi.org/ 10.1306/05220605164.
- Foster, G., Pogge von Strandmann, P.A., Rae, J., 2010. Boron and magnesium isotopic

- composition of seawater. G-cubed 11, 1–10. https://doi.org/10.1029/2010GC003201.
- Frimmel, H.E., 2009. Trace element distribution in Neoproterozoic carbonates as palaeoenvironmental indicator. Chem. Geol. 258 (3–4), 338–353. https://doi.org/10.1016/j.chemgeo.2008.10.033.
- Fritz, P., Smith, D., 1970. The isotopic composition of secondary dolomites. Geochem. Cosmochim. Acta 34 (11), 1161–1173. https://doi.org/10.1016/0016-7037(70)90056-6.
- Fu, X., Wang, J., Tan, F., Chen, M., Li, Z., Zeng, Y., Feng, X., 2016. New insights about petroleum geology and exploration of Qiangtang Basin, northern Tibet, China: a model for low-degree exploration. Mar. Petrol. Geol. 77, 323–340. https://doi.org/10.1016/j.marpetgeo.2016.06.015.
- Fu, X., Wang, J., Tan, F., Feng, X., Wang, D., He, J., 2013. Gas hydrate formation and accumulation potential in the Qiangtang Basin, northern Tibet, China. Energy Convers. Manag. 73, 186–194. https://doi.org/10.1016/j.enconman.2013.04.020.
- Galy, A., Yoffe, O., Janney, P.E., Williams, R.W., Cloquet, C., Alard, O., Halicz, L., Wadhwa, M., Hutcheon, I.D., Ramon, E., 2003. Magnesium isotope heterogeneity of the isotopic standard SRM980 and new reference materials for magnesium-isotope-ratio measurements. J. Anal. Atomic Spectrom. 18 (11), 1352–1356. https://doi.org/10.1039/B309273A.
- Geske, A., Goldstein, R.H., Mavromatis, V., Richter, D.K., Buhl, D., Kluge, T., John, C.M., Immenhauser, A., 2015. The magnesium isotope (8²⁶Mg) signature of dolomites. Geochem. Cosmochim. Acta 149, 131–151. https://doi.org/10.1016/j.gca.2014.11.003.
- J.gcd.2014.11.003.

 Geske, A., Zorlu, J., Richter, D., Buhl, D., Niedermayr, A., Immenhauser, A., 2012.

 Impact of diagenesis and low grade metamorphosis on isotope (δ²⁶Mg, δ¹³C, δ¹⁸O and ⁸⁷Sr/⁸⁶Sr) and elemental (Ca, Mg, Mn, Fe and Sr) signatures of Triassic sabkha dolomites. Chem. Geol. 332, 45–64. https://doi.org/10.1016/j.chemgeo.2012.09.014.
- Golonka, J., 2007. Late triassic and early jurassic palaeogeography of the world. Palaeogeogr. Palaeoclimatol. Palaeoecol. 244 (1–4), 297–307. https://doi.org/10.1016/j.palaeo.2006.06.041.
- Gomez-Rivas, E., Corbella, M., Martín-Martín, J., Stafford, S., Teixell, A., Bons, P.D., Griera, A., Cardellach, E., 2014. Reactivity of dolomitizing fluids and Mg source evaluation of fault-controlled dolomitization at the Benicassim outcrop analogue (Maestrat Basin, E Spain). Mar. Petrol. Geol. 55, 26–42. https://doi.org/10.1016/j.marpetgeo.2013.12.015.
- Gregg, J.M., Bish, D.L., Kaczmarek, S.E., Machel, H.G., 2015. Mineralogy, nucleation and growth of dolomite in the laboratory and sedimentary environment: a review. Sedimentology 62 (6), 1749–1769. https://doi.org/10.1111/sed.12202.
- Gregg, J.M., Howard, S.A., Mazzullo, S., 1992. Early diagenetic recrystallization of Holocene (< 3000 years old) peritidal dolomites, Ambergris Cay, Belize. Sedimentology 39 (1), 143–160. https://doi.org/10.1111/jj.1365-3091.1992.tb01027.x.
- Gregg, J.M., Sibley, D.F., 1984. Epigenetic dolomitization and the origin of xenotopic dolomite texture. J. Sediment. Res. 54 (3), 908–931. https://doi.org/10.1306/ 212F8535-2B24-11D7-8648000102C1865D.
- Haas, J., Budai, T., Győri, O., Kele, S., 2014. Multiphase partial and selective dolomitization of Carnian reef limestone (Transdanubian Range, Hungary). Sedimentology 61 (3), 836–859. https://doi.org/10.1111/sed.12088.
- Haeri-Ardakani, O., Al-Aasm, I., Coniglio, M., 2013. Petrologic and geochemical attributes of fracture-related dolomitization in Ordovician carbonates and their spatial distribution in southwestern Ontario, Canada. Mar. Petrol. Geol. 43, 409–422. https://doi.org/10.1016/j.marpetgeo.2012.12.006.
- Hallam, A., 2001. A review of the broad pattern of Jurassic sea-level changes and their possible causes in the light of current knowledge. Palaeogeogr. Palaeoclimatol. Palaeoecol. 167 (1–2), 23–37. https://doi.org/10.1016/S0031-0182(00)00229-7.
- Higgins, J.A., Schrag, D.P., 2015. The Mg isotopic composition of Cenozoic seawater evidence for a link between Mg-clays, seawater Mg/Ca, and climate. Earth Planet Sci. Lett. 416, 73—81. https://doi.org/10.1016/j.epsl.2015.01.003.
- Hu, Z., Han, Z., Ma, A., Xia, Z., Wang, L., Li, W., 2024. The covariation between MgC isotopes and trace elements in dolostones: implications for reconstructing the seawater chemistry. Sediment. Geol. 459, 106552. https://doi.org/10.1016/isedgep.2023.106552
- Hu, Z., Hu, W., Liu, C., Sun, F., Liu, Y., Li, W., 2019. Conservative behavior of Mg isotopes in massive dolostones: from diagenesis to hydrothermal reworking. Sediment. Geol. 381, 65–75. https://doi.org/10.1016/j.sedgeo.2018.12.007.
- Hu, Z., Hu, W., Wang, X., Lu, Y., Wang, L., Liao, Z., Li, W., 2017. Resetting of Mg isotopes between calcite and dolomite during burial metamorphism: outlook of Mg isotopes as geothermometer and seawater proxy. Geochem. Cosmochim. Acta 208, 24–40. https://doi.org/10.1016/j.gca.2017.03.026.
- Huang, K.J., Shen, B., Lang, X.G., Tang, W.B., Peng, Y., Ke, S., Kaufman, A.J., Ma, H.R., Li, F.B., 2015. Magnesium isotopic compositions of the Mesoproterozoic dolostones: implications for Mg isotopic systematics of marine carbonates. Geochem. Cosmochim. Acta 164, 333–351. https://doi.org/10.1016/j.gca.2015.05.002.
- Jacobsen, S.B., Kaufman, A.J., 1999. The Sr, C and O isotopic evolution of Neoproterozoic seawater. Chem. Geol. 161 (1–3), 37–57. https://doi.org/10.1016/ S0009-2541(99)00080-7.
- Jacobson, A.D., Zhang, Z., Lundstrom, C., Huang, F., 2010. Behavior of Mg isotopes during dedolomitization in the madison aquifer, south Dakota. Earth Planet Sci. Lett. 297 (3–4), 446–452. https://doi.org/10.1016/j.epsl.2010.06.038.
- Jarvis, I., Mabrouk, A., Moody, R.T., de Cabrera, S., 2002. Late Cretaceous (Campanian) carbon isotope events, sea-level change and correlation of the Tethyan and Boreal realms. Palaeogeogr. Palaeoclimatol. Palaeoecol. 188 (3–4), 215–248.

https://doi.org/10.1016/S0031-0182(02)00578-3.

- Jarvis, I., Murphy, A.M., Gale, A.S., 2001. Geochemistry of pelagic and hemipelagic carbonates: criteria for identifying systems tracts and sea-level change. J. Geol. Soc. 158, 685–696. https://doi.org/10.1144/jgs.158.4.685.
- Jiang, L., Cai, C., Worden, R.H., Crowley, S.F., Jia, L., Zhang, K., Duncan, I.J., 2016. Multiphase dolomitization of deeply buried Cambrian petroleum reservoirs, Tarim Basin, north-west China. Sedimentology 63 (7), 2130–2157. https://doi.org/10.1111/sed.12300.
- Jiang, L., Shen, A., Wang, Z., Hu, A., Wang, Y., Luo, X., Liang, F., Azmy, K., Pan, L., 2022.
 U–Pb geochronology and clumped isotope thermometry study of Neoproterozoic dolomites from China. Sedimentology 69 (7), 2925–2945. https://doi.org/10.1111/sed.13026.
- Kimmig, S.R., Nadeau, M.D., Swart, P.K., Holmden, C., 2021. Mg and Sr isotopic evidence for basin wide alteration of early diagenetic dolomite in the Williston Basin by ascending crustal fluids. Geochem. Cosmochim. Acta 311, 198–225. https://doi.org/10.1016/j.gca.2021.06.006.
- Koeshidayatullah, A., Corlett, H., Stacey, J., Swart, P.K., Boyce, A., Hollis, C., 2020. Origin and evolution of fault-controlled hydrothermal dolomitization fronts: a new insight. Earth Planet Sci. Lett. 541, 116291. https://doi.org/10.1016/ j.epsl.2020.116291.
- Kretz, R., 1982. A model for the distribution of trace elements between calcite and dolomite. Geochem. Cosmochim. Acta 46 (10), 1979–1981. https://doi.org/ 10.1016/0016-7037(82)90137-5.
- Lai, W., Hu, X., Garzanti, E., Xu, Y., Ma, A., Li, W., 2019. Early Cretaceous sedimentary evolution of the northern Lhasa terrane and the timing of initial Lhasa-Qiangtang collision. Gondwana Res. 73, 136–152. https://doi.org/10.1016/ i.gr.2019.03.016.
- Land, L.S., 1998. Failure to precipitate dolomite at 25 °C from dilute solution despite 1000-foldoversaturation after 32 years. Aquat. Geochem. 4, 361–368. https://doi.org/10.1023/A:1009688315854.
- Langmuir, D., Melchior, D., 1985. The geochemistry of Ca, Sr, Ba and Ra sulfates in some deep brines from the Palo Duro Basin, Texas. Geochem. Cosmochim. Acta 49 (11), 2423–2432. https://doi.org/10.1016/0016-7037(85)90242-X.
- Li, W., Bialik, O.M., Wang, X., Yang, T., Hu, Z., Huang, Q., Zhao, S., Waldmann, N.D., 2019. Effects of early diagenesis on Mg isotopes in dolomite: the roles of Mn (IV)-reduction and recrystallization. Geochem. Cosmochim. Acta 250, 1–17. https://doi.org/10.1016/j.gca.2019.01.029.
- Li, X., Zhu, G., Chen, Z., Li, T., Wang, S., Ai, Y., Zhang, Y., Tian, L., 2023. Mg isotopic geochemistry and origin of Early Ordovician dolomite and implications for the formation of high-quality reservoir in the Tabei area, Tarim Basin, NW China. I. Asian Earth Sci. 105757. https://doi.org/10.1016/j.iseaes.2023.105757.
- J. Asian Earth Sci. 105757. https://doi.org/10.1016/j.jseaes.2023.105757. Li, X., Zhu, G., Li, T., Zhou, L., Wu, Y., Tian, L., 2022. Mg isotopic characteristics and genetic mechanism of dolomite of Cambrian Xixiangchi Formation in central Sichuan Basin. Acta Pet. Sin. 43 (11), 1585–1603. https://doi.org/10.7623/syxb202211006 (in Chinese).
- Li, Z., Goldstein, R.H., Franseen, E.K., 2013. Ascending freshwater-mesohaline mixing: a new scenario for dolomitization. J. Sediment. Res. 83 (3), 277–283. https://doi.org/10.2110/jsr.2013.24.
- Lin, P., Peng, J., Zhang, L., Lan, X., Wang, J., Xia, Q., Xia, J., 2022. Characteristics of multiple dolomitizing fluids and the genetic mechanism of dolomite formation in the Permian Qixia Formation, NW Sichuan Basin. J. Petrol. Sci. Eng. 208, 109749. https://doi.org/10.1016/j.petrol.2021.109749.
- Liu, J.Q., Chen, W.B., Yang, P., Chen, W.X., Fu, X.G., 2008. The Longeni-Angdanrco paelo-oil dolomite geochemical characteristcs in southern part of the central uplift zone or Qiangtang basin and it's significance. Acta Petrol. Sin. 24 (6), 1379–1389.
- Lumsden, D.N., 1988. Characteristics of deep-marine dolomite. J. Sediment. Res. 58 (6), 1023–1031. https://doi.org/10.1306/212F8EEF-2B24-11D7-8648000102C1865D.
- Ma, A., Hu, X., Garzanti, E., Boudagher-Fadel, M., Xue, W., Han, Z., Wang, P., 2023. Paleogeographic and tectonic evolution of mesozoic qiangtang basins (Tibet). Tectonophysics 862, 229957. https://doi.org/10.1016/j.tecto.2023.229957.
- Ma, A., Hu, X., Garzanti, E., Han, Z., Lai, W., 2017. Sedimentary and tectonic evolution of the southern Qiangtang basin: implications for the Lhasa-Qiangtang collision timing. J. Geophys. Res. Solid Earth 122, 4790–4813. https://doi.org/10.1002/ 2017IR014211
- Ma, Y., Guo, T., Zhao, X., Cai, X., 2008. The formation mechanism of high-quality dolomite reservoir in the deep of Puguang Gas Field. Sci. China Earth Sci. 51, 53–64. https://doi.org/10.1007/s11430-008-5008-y.
- Machel, H.G., 2004. Concepts and models of dolomitization: a critical reappraisal. In: Geological Society, vol. 235. Special Publications, London, pp. 7–63. https://doi.org/10.1144/GSL.SP.2004.235.01.02.
- Natalicchio, M., Pierre, F.D., Birgel, D., Brumsack, H., Carnevale, G., Gennari, R., Gier, S., Lozar, F., Pellegrino, L., Sabino, M., 2019. Paleoenvironmental change in a precession-paced succession across the onset of the Messinian salinity crisis: insight from element geochemistry and molecular fossils. Palaeogeogr. Palaeoclimatol. Palaeoecol. 518, 45–61. https://doi.org/10.1016/j.palaeo.2019.01.009.
- Nicholls, G., 1967. Trace elements in sediments: an assessment of their possible utility as depth indicators. Mar. Geol. 5 (5–6), 539–555. https://doi.org/10.1016/
- Ning, M., Huang, K., Lang, X., Ma, H., Yuan, H., Peng, Y., Shen, B., 2019. Can crystal morphology indicate different generations of dolomites? Evidence from magnesium isotopes. Chem. Geol. 516, 1–17. https://doi.org/10.1016/ j.chemgeo.2019.04.007.
- Nothdurft, L.D., Webb, G.E., Kamber, B.S., 2004. Rare earth element geochemistry of

Late Devonian reefal carbonates, Canning Basin, Western Australia: confirmation of a seawater REE proxy in ancient limestones. Geochem. Cosmochim. Acta 68 (2), 263–283. https://doi.org/10.1016/S0016-7037(03)00422-8.

- Pan, G., Wang, L., Li, R., Yuan, S., Ji, W., Yin, F., Zhang, W., Wang, B., 2012. Tectonic evolution of the Qinghai-Tibet plateau. J. Asian Earth Sci. 53, 3–14. https:// doi.org/10.1016/j.jseaes.2011.12.018.
- Pullen, A., Kapp, P., Gehrels, G.E., Vervoort, J.D., Ding, L., 2008. Triassic continental subduction in central Tibet and mediterranean-style closure of the Paleo-Tethys Ocean. Geology 36 (5), 351–354. https://doi.org/10.1130/G24435A.1.
- Qing, H., Qiao, Z., Zhang, S., Cosford, J., Hu, A., Liang, F., Wang, Y., Zheng, J., 2023. $\delta^{26} \text{Mg} \delta^{13} \text{C-} \delta^{18} \text{O}$ systems as geochemical tracers for dolomite recrystallization: a case study of lower Ordovician dolomite from Tarim Basin. Chem. Geol. 619, 121302. https://doi.org/10.1016/j.chem.geo.2023.121302.
- Ryan, B.H., Kaczmarek, S.E., Rivers, J.M., 2020. Early and pervasive dolomitization by near-normal marine fluids: new lessons from an Eocene evaporative setting in Qatar. Sedimentology 67 (6), 2917–2944. https://doi.org/10.1111/sed.12726.
- Ryb, U., Eiler, J.M., 2018. Oxygen isotope composition of the Phanerozoic ocean and a possible solution to the dolomite problem. Proc. Natl. Acad. Sci. USA 115 (26), 6602–6607. https://doi.org/10.1073/pnas.1719681115.
- Sena, C.M., John, C.M., Jourdan, A.-L., Vandeginste, V., Manning, C., 2014. Dolomitization of lower cretaceous peritidal carbonates by modified seawater: constraints from clumped isotopic paleothermometry, elemental chemistry, and strontium isotopes. J. Sediment. Res. 84 (7), 552–566. https://doi.org/10.2110/isr.2014.45.
- Shen, A., Hu, A., Cheng, T., Liang, F., Pan, W., Feng, Y., Zhao, J., 2019. Laser ablation in situ U-Pb dating and its application to diagenesis-porosity evolution of carbonate reservoirs. Petrol. Explor. Dev. 46 (6), 1127–1140. https://doi.org/ 10.11698/PFD.2019.06.05
- Sibley, D.F., Gregg, J.M., 1987. Classification of dolomite rock textures. J. Sediment. Res. 57 (6), 967–975. https://doi.org/10.1306/212F8CBA-2B24-11D7-8648000102C1865D.
- Stoll, H.M., Schrag, D.P., 2001. Sr/Ca variations in Cretaceous carbonates: relation to productivity and sea level changes. Palaeogeogr. Palaeoclimatol. Palaeoecol. 168 (3–4), 311–336. https://doi.org/10.1016/S0031-0182(01)00205-X.
- Teng, F.Z., 2017. Magnesium isotope geochemistry. Rev. Mineral. Geochem. 82 (1), 219–287. https://doi.org/10.2138/rmg.2017.82.7.
- Tostevin, R., Shields, G.A., Tarbuck, G.M., He, T., Clarkson, M.O., Wood, R.A., 2016. Effective use of cerium anomalies as a redox proxy in carbonate-dominated marine settings. Chem. Geol. 438, 146–162. https://doi.org/10.1016/j.chemgeo.2016.06.027.
- Veizer, J., Ala, D., Azmy, K., Bruckschen, P., Buhl, D., Bruhn, F., Carden, G.A., Diener, A., Ebneth, S., Godderis, Y., 1999. $^{87}\text{Sr}/^{86}\text{Sr}$, $\delta^{13}\text{C}$ and $\delta^{18}\text{O}$ evolution of Phanerozoic seawater. Chem. Geol. 161 (1–3), 59–88. https://doi.org/10.1016/S0009-2541(99)00081-9.
- Wan, Y., Wang, J., Fu, X., 2020. Geochemical tracing of isotopic fluid of dolomite reservoir in the Middle Jurassic Buqu Formation in southern depression of Qiangtang Basin. Oil Gas Geol. 41 (1), 189–200. https://doi.org/10.11743/ogg20200117 (in Chinese).
- Wan, Y., Wang, J., Wan, F., Fu, X., Wang, Z., Shen, L., 2017. Characteristics and indications of rare earth elements in carbonates in the Buqu Formation, southern Qiangtang Basin. Petrol. Geology Experi. 39 (5), 654–665. https://doi.org/10.11781/sysydz201705655 (in Chinese).
- Wang, J., Fu, X., Wei, H., Zheng, B., Wang, Z., Shen, L., Mansou, A., 2024. An overview of the Qiangtang Basin: geology, hydrocarbon resources and the role of the Tethyan evolution. J. Asian Earth Sci. 106128. https://doi.org/10.1016/j.jseaes.2024.106128.
- Wang, J., Wang, Z., Fu, X., Song, C., Tan, F., Wei, H., 2022. New discoveries on the first petroleum scientific drilling (QK-1) of the Qiangtang Basin, Tibetan Plateau. Chin. Sci. Bull. 67 (3), 321–328. https://doi.org/10.1360/TB-2021-1048 (in Chinese).
- Wang, P., Wang, G., Chen, Y., Hao, F., Yang, X., Hu, F., Zhou, L., Yi, Y., Yang, G., Wang, X., 2023. Formation and preservation of ultra-deep high-quality dolomite reservoirs under the coupling of sedimentation and diagenesis in the central Tarim Basin, NW China. Mar. Petrol. Geol. 149, 106084. https://doi.org/10.1016/j.marpetgeo.2022.106084.
- Wang, Y., Shi, Z., Qing, H., Tian, Y., Gong, X., 2021. Petrological characteristics, geochemical characteristics, and dolomite model of the lower cambrian Long-wangmiao Formation in the periphery of the Sichuan Basin, China. J. Petrol. Sci. Eng. 202, 108432. https://doi.org/10.1016/j.petrol.2021.108432.
- Warren, J., 2000. Dolomite: occurrence, evolution and economically important associations. Earth Sci. Rev. 52 (1–3), 1–81. https://doi.org/10.1016/S0012-8252(00)00022-2.
- Wei, T., Cai, C., Hu, Y., Yu, H., Liu, D., Jiang, Z., Wang, D., 2023. Nature and evolution of diagenetic fluids in the deeply buried cambrian xiaoerbulake formation, Tarim Basin, China. Aust. J. Earth Sci. 70 (1), 126–144. https://doi.org/10.1080/ 08120099.2022.2122080.
- Wu, Z., Ji, C., Zhao, Z., Chen, C., 2020. Buried depth evolution and hydrocarbon generation history of the Jurassic System in central Qiangtang Basin. Acta Geol. Sin. 94 (10), 2823–2833. https://doi.org/10.19762/j.cnki.dizhixuebao.2020095 (in Chinese).
- Xia, G., Ji, C., Yang, W., Wu, C., Yi, H., Zhang, S., Li, Q., Li, G., Li, 2016. Fluid inclusions characteristics and hydrocarbon charging history of oil reservoir belt in the Mid-Jurassic Buqu Formation, Southern Qiangtang depression. Acta Pet. Sin. 37 (10), 1247. https://doi.org/10.7623/syxb201610004 (in Chinese).
- Xu, H., Qin, J., 2004. Thermal evolution history of the Mesozoic marine source rock

in the Qiangtang Basin, Tibet. Petrol. Explor. Dev. 31 (2), 59–63. https://doi.org/10.3321/j.issn:1000-0747.2004.02.016 (in Chinese).

- Xue, W., Hu, X., Ma, A., Garzanti, E., Li, J., 2020. Eustatic and tectonic control on the evolution of the jurassic north qiangtang basin, northern Tibet, China: impact on the petroleum system. Mar. Petrol. Geol. 120, 104558. https://doi.org/ 10.1016/j.marpetgeo.2020.104558.
- Yang, X., Fan, T., Tang, S., Li, J., Meng, M., Hu, P., 2017. Sedimentology and sequence stratigraphy of evaporites in the middle jurassic Buqu Formation of the qiangtang basin, Tibet, China. Carbonates Evaporites 32, 379–390. https://doi.org/10.1007/s13146-016-0324-3.
- Yi, H., Chen, Z., Ji, C., Yang, X., Xia, G., Wu, C., 2014. New evidence for deep burial origin of sucrosic dolomites from Middle Jurrasic Buqu Formation in southern Qiangtang basin. Acta Petrol. Sin. 30 (3), 737–746 (in Chinese).
- Zenger, D.H., 1983. Burial dolomitization in the Lost Burro Formation (Devonian),

- east-central California, and the significance of late diagenetic dolomitization. Geology 11 (9), 519–522. https://doi.org/10.1130/0091-7613(1983)11<519: BDITLB>2.0.CO;2.
- Zhao, W., Shen, A., Qiao, Z., Pan, L., Hu, A., Zhang, J., 2018. Genetic types and distinguished characteristics of dolomite and the origin of dolomite reservoirs. Petrol. Explor. Dev. 45 (6), 983–997. https://doi.org/10.1016/S1876-3804(18) 30103-4
- Zhu, D.C., Zhao, Z.D., Niu, Y., Dilek, Y., Hou, Z.Q., Mo, X.X., 2013. The origin and pre-Cenozoic evolution of the Tibetan Plateau. Gondwana Res. 23 (4), 1429–1454. https://doi.org/10.1016/j.gr.2012.02.002.
- Zhu, G., Li, X., Li, T., Zhou, L., Wu, Y., Shen, B., Ning, M., 2023. Genesis mechanism and Mg isotope difference between the sinian and cambrian dolomites in Tarim Basin. Sci. China Earth Sci. 66 (2), 334–357. https://doi.org/10.1007/s11430-021-1010-6